공학박사 학위논문

Dynamic Expansion and Trapping of Electrons in Magnetically Expanding Plasma

자기적으로 팽창하는 플라즈마에서 전자의 동적 팽창 및 구속 연구

2019 년 8 월

서울대학교 대학원

에너지시스템공학부

김 준 영

Dynamic Expansion and Trapping of Electrons in Magnetically Expanding Plasma

지도교수 황 용 석

이 논문을 공학박사 학위논문으로 제출함

2019 년 8 월

서울대학교 대학원

에너지시스템공학부

김 준 영

김준영의 공학박사 학위논문을 인준함

2019 년 8 월

위 원 장	정 경 재	(인)
부위원장	황 용 석	(인)
위 원	나 용 수	(인)
위 원	최 원 호	(인)
위 원	윤 건 수	(인)

Abstract

Dynamic Expansion and Trapping of Electrons in Magnetically Expanding Plasma

June Young Kim

Department of Energy Systems Engineering

The Graduate School

Seoul National University

Since the principle by which electrons are cooled in a divergent magnetic field is fundamental to the understanding of the electron kinetic property, thermodynamic analysis of electrons through the polytropic equation has attracted a great attention from astrophysics to applications for the purpose of space electric propulsion. Especially, experiments with laboratory-level plasmas with a magnetic nozzle (MN) that exhibit characteristics similar to the space plasmas are of great significance in that they can help deepen understanding of the magnetically expanding plasmas, providing various experimental and theoretical findings. In the case of electrodeless thruster, the MNs are proposed as next-generation electric propulsion system due to

its advantages in terms of contactless operating driven by the magnetic confinement of the plasma stream, and versatile structure and strength of magnetic field which can be modified in-flight. Accordingly, there has been a significant interest in the MN to elucidate the physics of plasmas expanding in divergent magnetic fields for space plasma and electric propulsion systems.

In the sense that a conversion of the electron momentum to the ion kinetic energy determines the characteristics of the MN, fundamental research on the kinetic feature of a magnetically expanding plasma has focused on the thermodynamic property of electrons and proposed directions to the desired application. Unlike the common perception of this importance, various research groups have proposed contradictory arguments based on their theoretical approaches regarding the thrust efficiency from the viewpoint of heat flow of electrons.

In essence, the evolution of electrons along the divergent magnetic field is an adiabatic process with γ_e of 5/3 in collisionless plasmas. However, in recent experiments, a linear regression of the measured plasma parameters along magnetically expanding nozzle has presented γ_e of less than adiabatic ($\gamma_e = 5/3$), rather closer to isothermal ($\gamma_e = 1$). The non-adiabatic behavior of the electrons observed in each experimental group has become a subject of interest while the rationale for the different states remains insufficient and theoretical consensus has not been reached.

In this thesis, thermodynamics of a magnetically expanding plasma has been investigated considering the existence of trapped electrons bouncing back and forth inside an effective potential well formed by a combination of external magnetic field

and self-generating ambipolar electrostatic potential. The properties of trapped electrons are distinguished from that of the adiabatically expanding electrons with $\gamma_e = 5/3$ by the separate measurement of each species using a double-sided planar Langmuir probe. Relationship between the electron pressure versus electron density averaged over electron energy probability functions (EEPFs) clearly reveals that the trapped electrons in the MN have a nearly isothermal characteristic. Existence of isothermally behaving trapped electrons together with adiabatically expanding electrons separates the MN system into two regions with different thermodynamic properties; one is a nearly adiabatic region located near the nozzle throat and the other is nearly isothermal region located in the downstream. A transition of electron thermodynamic property along a distance from the nozzle throat can be explained with conservation of magnetic moment of electrons bounced back by ambipolar electrostatic potential. Coexistence of the nearly adiabatic electrons with Maxwellian EEPF and the nearly isothermal electrons with high-energy-depleted EEPF makes the overall EEPF shape low-energy-populated EEPF, indicating a need for careful analysis on the measured EEPFs near the nozzle throat. In spite of significant contribution of trapped electrons to EEPF and overall electron thermodynamics, it is found that the trapped electrons behaving isothermally do not contribute to the generation of ambipolar electrostatic potential near the nozzle throat which is important for ion acceleration in the MN. The present study suggests that thrust efficiency should not be directly inferred from the value of polytropic exponent γ_e because thermodynamic property of a MN is influenced by isothermally behaving trapped electrons as well as adiabatically expanding electrons.

Additionally, we focus on the fact that the latest laboratory experiments have been limited to static observations and have restricted the analysis of the causes of the difference in the thermodynamic properties. In response to this problem, time-resolved measurement of the EEPFs is performed to reveal time-dependent kinetic property of magnetically expanding plasmas in the MN and grasp a detailed series of expansion processes in order to elucidate the electron thermodynamics. Through observation of the expansion process, it has been revealed that the effective potential well gradually formed by the self-generated electric field acts as a limiting factor in the motion of electrons; this effect attributes to the changes of the electron energy distribution represented as the accumulation of the trapped electrons. The accumulation over the entire region diminishes the degree of the cooling rate of a system. Furthermore, as the plasma potential gradient is gradually generated, the downstream region becomes disconnected from the source which eventually decreases the electric field in the downstream region initially generated by the adiabatic expansion. The present study emphasizes that the kinetic features of a MN is strongly affected by the non-stationary motion of the trapped electrons; thus, the temporal behavior of the trapped electrons must be considered for prediction and analysis of magnetically expanding plasmas.

Keywords; Magnetically expanding plasma, Electric propulsion, Electron thermodynamics, Polytropic equation, Non-adiabatic behavior, Magnetic mirror, Electron energy probability function, Solar wind

Student Number: 2015-30290

Contents

List of Figures

List of Tables

List of Abbreviations

e	: Elementary charge
B_z	: Axial magnetic field strength
B_{Max}	: Axial magnetic field strength at center of nozzle throat
E	: Electric field
E_e	: Total electron energy
ε	: Average energy lost per electron-ion pair leaving source exit
ε_e	: Electron enthalpy
ε_{ef}	: Electron energy flow to boundary of source exit
ε_i	: Ion kinetic energy
$f_{c,\alpha}$,	: Particle cyclotron frequency
f_e	: Electron energy probability function
f_i	: Ion energy distribution function
F	: Thrust determined by final ion exhaust velocity
g_e	: Electron energy distribution function
I_c	: Collector current
I_e	: Probe current
L_B	: Characteristics scale length of magnetic field inhomogeneity
$\mathrm{L}_{D,\alpha}$	: Drift scale length of particle
$\dot{m}$	: Total mass flow rate
m_i	: Ion mass
n	: Degree of freedom
n_e	: Electron density
p_e	: Electron pressure

p_{e0} : Electron pressure at center of nozzle throat

P_a : Actual power emerging from source exit

P_{in} : Total input power to plasma source

P_k : Maximum kinetic power

P_l : Total loss power in plasma source

Q_e : Electron power lost to magnetic field aligned heat conduction

T_{bulk} : Bulk electron temperature

T_e : Electron temperature

$T_{\parallel,e0}$: Electron temperature parallel to axial magnetic field at source exit

$T_{\perp,e0}$: Electron temperature perpendicular to axial magnetic field at source exit

T_{eff} : Effective electron temperature

T_{tail} : Tail electron temperature

V_{beam} : Beam potential

V_{bias} : Probe bias voltage

V_d : Discriminator voltage

V_p : Plasma potential

$\Delta V_{p,total}$: Total plasma potential drop along axial direction

$V_{p,\mathrm{I}}$: Plasma potential at Region I

$V_{p,\mathrm{II}}$: Plasma potential at Region II

V_G : Voltage applied to mesh grid

$v_{z,\alpha}$: Particle velocity in z-direction

$v_{\parallel,e}$: Electron velocity components parallel to magnetic field

$v_{\perp,e}$: Electron velocity components perpendicular to magnetic field

β : Plasma beta

γ_e	: Polytropic index
η	: Thrust efficiency
λ_d	: Debye length
μ_e	: Magnetic moment of electron
μ_{e0}	: Magnetic moment at the center of nozzle throat
$\mu_{e,m}$	: Maximum magnetic moment of electron
τ_i	: Ion plasma time
$\tau_{en,elastic}$	: Elastic collision time with atom
$\tau_{en,ion}$	: Ionization collision time with atom
$\tau_{escaping}$	: Particle escaping time
τ_{Max}	: Averaging time for electron to suffer 100% change in energy via electron-electron collision
ψ	: Magnetic flux surface

Chapter 1. Introduction

In recent years, there has been a growing interest in the flow of plasma through magnetic nozzle (MN) to analyze various research fields such as plasma jet thrusters for spacecraft [1-8], and solar wind from the sun [9-11]. Particularly, in the case of electrodeless thruster, MNs are proposed as next-generation electric propulsion system due to its advantages in terms of 1) contactless operating due to the magnetic confinement of the plasma stream assuring long lifetime without erosion of generation and acceleration electrode, and 2) versatile structure and strength of magnetic field which can be modified in-flight [12-16]. Accordingly, there has been a significant interest in the MN to elucidate the physics of plasmas expanding in divergent magnetic fields for electric propulsion systems [17-25].

The magnetic field structure in a MN is similar to the convergent-divergent solid wall of a de-Laval nozzle employed in order to provide neutral gases accelerated to super-sonic exhaust velocity. Like the de Laval nozzle, the MN device converts the thermal energy of the plasma into directed kinetic energy, and unlike the physical wall of the de Laval nozzle, the desired thrust is achieved by the kinetic behavior of the charged particles in the guiding magnetic field; thus, the MN devices require an overall understanding of plasma physics. Especially, the thrust application as an electron-driven MN is based on the following mechanism. First of all, complex heating and transport mechanisms in the plasma source (e.g., the helicon and electron cyclotron resonance sources) make the electrons possess a high thermal energy to obtain large exhaust velocity of ions and determine the shape of the electron energy distributions at the nozzle throat. Secondly, the electron cooling process in an expanding magnetic field, which guiding the electrons to prevent undesired diffusion, contributes to the formation of the ambipolar electric field (thrust generation). Thirdly, based on the closed nature of the magnetic field lines, the MN system requires a detachment process in the downstream region (i.e., separation of plasmas from the divergent magnetic field line) to acquire the thrust gain and keep the plume divergence

angle low to prevent damage to the MN peripherals [27]. In addition, interaction between the plasma current and the magnetic field during the expansion process causes various physical phenomena, represented as an electron diamagnetic current effect on the axial plasma momentum [19]. Due to the characteristics of plasma dynamics, all aspects mentioned above, including the internal energy of the plasma in the upstream source and the process of plasma change in the downstream region, are strongly related to each other. Accordingly, a lot of efforts have been made to understating the characteristics of the MN relying on the various operating conditions by combining plasma modeling and experiment [12-27].

1.1. Electron Heat Transfer in Performance Scaling of Magnetic Nozzle

The goal of this chapter is to recognize the importance of the electron heat conduction term in modeling for performance scaling of the MN devices. Generally, thrust efficiency η is defined as the ratio of the maximum kinetic power P_k to total input power to plasma source P_{in} as follows [28]

$$\eta = \frac{P_k}{P_{in}} = \frac{F^2}{2\dot{m}P_{in}}, \tag{1.1}$$

where F is the thrust determined by the final ion exhaust velocity in the downstream region, $\dot{m}$ is the total mass flow rate, respectively. The actual power emerging from the source exit P_a can be derived from P_{in} with the relation $P_{in} = P_a + P_l$ by considering the total loss power in the source P_l removed from the plasmas through the sheath and the inelastic collision with the incoming propellant [Fig. 1.1]. After all, P_a is the function of the average energy lost per electron-ion pair ε leaving the source exit. In the case of electron, the electron energy flow to the boundary of the source exit ε_{ef} can be estimated through average energy loss per electron at the source exit expressed as the sum of enthalpy and heat flows as follows [29,30]

$$\varepsilon_{ef} = \frac{3}{2}T_{\parallel,e0} + T_{\perp,e0} + \frac{mQ_e}{\dot{m}}, \tag{1.2}$$

where $T_{\parallel,e0}$ and $T_{\perp,e0}$ are the electron temperature parallel and perpendicular to the axial magnetic field at the source exit, respectively, and Q_e is the electron power lost to magnetic field aligned heat conduction. The potential energy along a magnetic field line can be assumed as constant at the source region; thus, enthalpy consists of only thermal energy components $T_{e0} = T_{\parallel,e0} + 2T_{\perp,e0}$ considering the degree of freedom of electrons.

The above equations indicate that the thermal energy and heat conduction of electrons determined in the boundary between the source and expansion regions (i.e., source exit) directly contributes to the thermal conversion efficiency. Accordingly, importance of the determination of the electron thermodynamic properties has been

emphasized in MN modeling and experimental work performed so far [29-33]. As an initial study for the evaluation of a MN performance, Andersen et al. [31] modified the magnetic field structure of the Q-device to a magnetic de-Laval structure to generate a super-sonic plasma flow, and the experimental result was compared to that of plasma 1-D modeling based on the assumption of isothermally behaving electrons with the Boltzmann relation (i.e., $Q_e = \infty$). In contrast, the adiabatic process assumption ($Q_e = 0$) with slowly varying time-dependent ambipolar electric field was considered for analytical study of the dynamics of plasma in the divergent magnetic field [32].

Unlike the above studies, arbitrary determination of Q_e through introduction of the polytropic index as free parameter can facilitate the modeling work by proving certain information on plasma process. For example, in astrophysics, the Earth's bow shock standoff distance can be directly detected experimentally by adopting the artificially selected polytropic index [33]. Similarly, in previous thruster models, the performance scaling regarding the final exhaust velocity and the detachment efficiency have been analyzed along with equation of motion, where the polytropic index was treated as a free parameter deduced from experimental values [14,29].

In summary, the previous studies have succeeded in simplifying the energy equation by use of the polytropic equation in theoretical and engineering aspects of research regarding the magnetically expanding plasma. The arbitrary selected polytropic index as a free parameter for the determination of the field-aligned heat conduction has contributed to revealing various physical phenomena with significant meaning in astrophysics and thrust modeling.

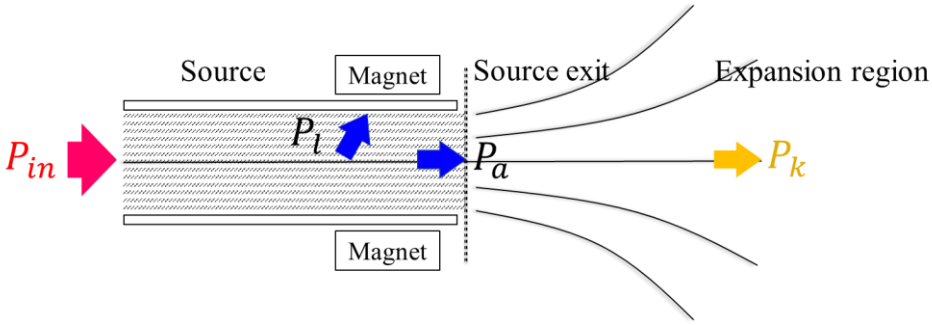

Figure 1.1. Geometry of the MN device. In the source volume, a plasma is generated by the input power P_{in}, which is divided into 1) the total loss power in the source P_l removed from the plasmas through the sheath and the inelastic collision with the incoming propellant and 2) the actual power emerging from the source exit P_a. Finally, the maximum kinetic power P_k represents the final ion exhaust velocity in the expansion region.

1.2. Polytropic Equation

In magnetically expanding plasmas, the polytropic state equation describes the ambipolar ion acceleration through a MN by relating the electron momentum equation and adiabatic equation of state. The polytropic exponent γ_e in the equation describes the exchange of heat between a magnetically expanding plasma and the system, and various kinetic simulations have been established to explore the physical meaning of MN devices by relating the thermodynamic model to the MN phenomena (e.g., plasma detachment, plume divergence efficiency, and thruster gain) [34-43].

For an electron gas in the collisionless condition, where only interactions between particles are perfectly elastic collisions, the evolution of the electron gas along magnetic field line can be modeled with a polytropic law;

$$T_e = C_e(\psi) n_e^{\gamma_e - 1}, \tag{1.3}$$

where T_e, n_e, γ_e is the electron temperature, electron density, and polytropic index, respectively. Since the electron gas is strongly magnetized in the absence of collisions with nearby field-aligned electrons, a constant $C_e(\psi) = T_{e0}/(n_{e0})^{\gamma_e - 1}$, where magnitudes with sub index 0 are evaluated at the origin, can be defined by the origin condition of each magnetic field flux surface ψ with the assumption of the axis symmetry. Thereby, the polytropic law of the electron gas in a MN system can be written as

$$\frac{T_e}{T_{e0}} = \left(\frac{n_e}{n_{e0}}\right)^{\gamma_e - 1}. \tag{1.4}$$

The polytropic index γ_e is equal to unity for the isothermal and equal to the specific heat ratio $(n+2)/n$, where n is the degree of freedom (i.e., $n = 3$ for monatomic gas). As one indicated, the introduction of γ_e from classical gas dynamics to the astrophysics permits the theoretical scientists to utilize the simplified mathematical shape of the energy equation in the MHD equation [10].

1.3. Objectives

In essence, the evolution of electrons along the divergent magnetic field is regarded as an adiabatic process with γ_e of 5/3 in collisionless MN devices. However, in recent experiments, a linear regression of the measured plasma parameters along magnetically expanding nozzle has presented γ_e of less than adiabatic ($\gamma_e = 5/3$), rather closer to isothermal ($\gamma_e = 1$) [40-44]. Each group has different argument in terms of improving the performance of the MNs by explaining a cause of measured γ_e lower than the adiabatic value. Little and Choueiri [40] suggested the possibility of performance improvements, arguing that the particle motion does not correspond to adiabatic cooling, but rather isothermal behavior reflected in the excessively small Nusselt number in which electron heat conduction along the magnetic field overwhelms convection, which was originally derived by Litvinov [42]. On the contrary, Takahashi et al. and Zhang et al. [41,44] concluded that the nozzle device with electric double layer is already in adiabatic expansion, which ensures no heat transfer into the system, and non-local electron kinetics very far from a local thermodynamic equilibrium for a nearly collisionless plasma is responsible for the low γ_e value. Even though the explanations of above groups are successful to interpret their own experimental results, the correlation between the change in γ_e and the nozzle characteristics that will support their claims on the fundamental understanding on the different value of γ_e is still not given in laboratory experiments.

Theoretically, kinetic approaches to the motion of electron and ion in the MN system divide the electrons into several groups according to their magnetic moment and total energy with a given plasma potential and magnetic field structure in the MN [35]. The model assumed the conservation of the adiabatic invariants of the electrons in a decreasing plasma potential that eventually tended to asymptotic values with non-isothermal cases as bounded plasma in magnetically diverging structure. Among the groups, the trapped electrons bounce back and forth in the MN similar to magnetic mirror within bounce back points of local maximum magnetic moment. By reflecting

the classification of electron groups, the model has associated the trapped motion of electrons and γ_e scales with multiple polytropic laws in a bounded collisionless plasmas [36]. The existence of trapped electrons in the MN structure seems to be theoretically clear, and thus relating the polytropic equation to the spatial evolution of trapped electrons is indispensable element in exploring the MN property. However, various groups of electrons classified by their total energy and magnetic moment have never been considered in the interpretation of experimentally measured polytropic exponent.

In this study, we introduce a double-sided planar Langmuir probe to measure the properties of electrons bounced back by the ambipolar potential separately from the properties of electrons ejected from the nozzle. Thermodynamic properties of electrons collected on each side are analyzed by the relationship between the electron pressure versus electron density averaged over EEPFs. The change in thermodynamic property of the system is also investigated by controlling the width of potential well depending on the magnetic field strength. In this thesis, we will show that the adiabatically expanding electrons with γ_e of $5/3$ and the trapped electrons behaving isothermally with γ_e of almost 1 can coexist near the nozzle throat, leading to the overall decrease of the measured γ_e. Using this finding, we explain the origin of non-Maxwellian distribution of electrons measured near the nozzle throat. Then, we investigate a role of the trapped electrons on the formation of ambipolar potential which is important for ion acceleration in MN.

Furthermore, we point out that the main reason for the absence of a theoretical consensus for the improvements of the MN efficiency arises from the lack of the clear interpretation of the plasma properties by focusing only on the final state of the electrons. Therefore, time-dependent kinetic property of magnetically expanding plasmas is investigated in order to overcome the limitations of analytical approach. The observation of the time evolution of the electron energy distribution is believed to provide a clue as to the understanding of the electron kinetic property along the magnetic field that has yet to be theoretically agreed upon.

Chapter 2. Experimental Setup and Diagnostics

2.1. Magnetic Nozzle

2.1.1 ECR Magnetic Nozzle

The experimental device and magnetic field structure used in the ECR MN [Figs. 2.1(a) and (b)] consists of three main components: 1) driver region including an electron cyclotron resonance (ECR) plasma source operating at frequency 2.45 GHz; 2) nozzle area where the magnetically converging and diverging field is formed; 3) plasma diffusion region where a cylindrical chamber is surrounded by a pair of solenoid coils for generating various curved MN structures [45].

In the driver region, a magnetic field of 875 Gauss is generated by two identical solenoid coils axially placed on the cylindrical chamber; currents of two ECR magnets (EF1 and EF2) are fixed at 60 A. A direct current from 50 A to 200 A is applied to nozzle field magnet (NF) to control the strength and configuration of magnetic field in the diffusion region. generate convergent and divergent MN structure. In most experiments, guiding magnets (GF1 and GF2) are turned off, except for the generation of stretched field where currents of 55 A is applied to both coils to produce nearly uniform magnetic field near 200 G in the diffusion region. A 600 W microwave power input from a 2.45 GHz magnetron (ASTEX, FI20061) is injected through a WR284 waveguide along with the axial magnetic field direction at the maximum field position for high-field-side launce to avoid the cut-off for the right hand circularly polarized wave (R-wave). The impedance between the source and the load is automatically matched by an auto-matching system (ASTEX, SmartMatch™). A vacuum pumping system consists of a 350 L/min oil-sealed rotary pump and a 1000 L/sec turbo molecular pump. Using a mass flow controller with a maximum flow rate of 50 mL/min, argon gas is injected through a gas feeding port at a distance -23 cm from

the nozzle throat. The base pressure is 8.0×10^{-7} and the operating argon pressure is fixed at 4.5×10^{-4} Torr.

After analyzing the characteristics of the ECR MN according to the strength of the magnetic field, a mesh grid (12-line per inch) is mounted in the ECR MN under the goal of the plasma property control in the plasma diffusion region [Fig. 2.2]. The mesh grid is located at -6 cm from the nozzle throat (between the ECR layer and the nozzle throat) to prevent ionization during the magnetic expansion and biased by the DC voltage V_G with respect to the chamber ground. An input power injected to plasma is fixed at 800 W. The base pressure is 5.0×10^{-6} Torr and the operating argon pressure is fixed at 2.0×10^{-4} Torr.

Table 1. Main parameters of the ECR MN device [45].

Parameters		Specification
Microwave Frequency [GHz]		2.45
Max. Microwave Power [kW]		1.5
Driver Chamber [m]		$0.15\ (D) \times 0.42\ (L)$
Diffusion Chamber [m]		$0.60\ (D) \times 0.66\ (L)$
Gas Species		Argon
Max. Magnetic Field Strength at Axial Center of Coil [G]	EF1 and EF2 Coils	1500 (80 A)
	NF Coil	970 (250 A)
	GF1 and GF2 Coils	190 (120 A)
DC Voltage Applied to Mesh Grid [V]		-30 to 25

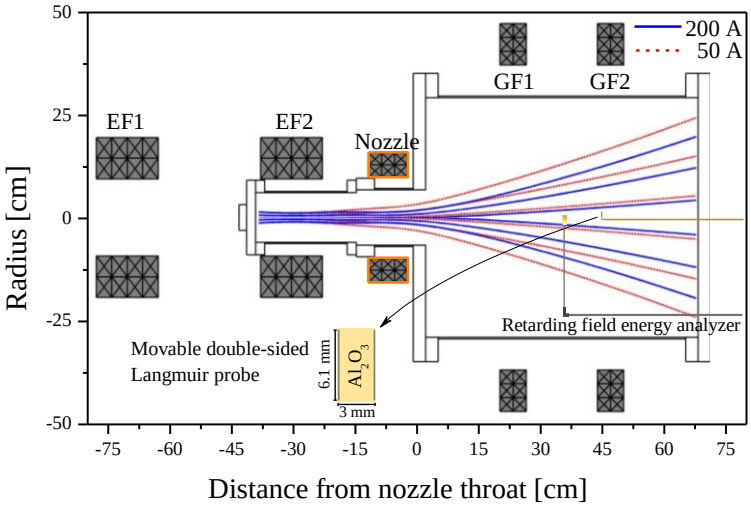

(a)

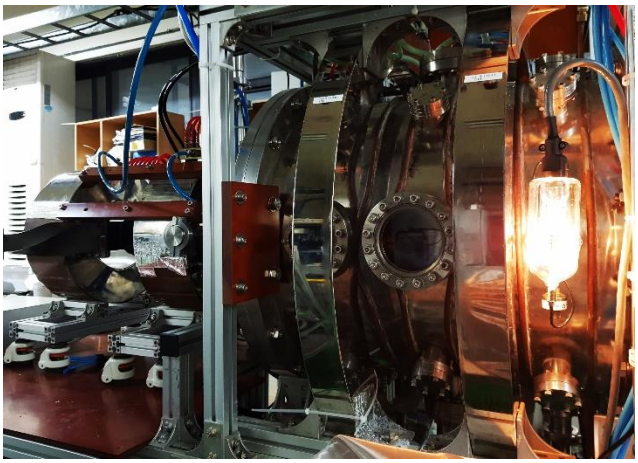

(b)

Figure 2.1. (a) Schematic diagram of the axially symmetric MN showing the ECR plasma source region and the divergent magnetic field configuration with axially movable double-sided Langmuir probe and retarding field energy analyzer, and (b) photo of the ECR nozzle device.

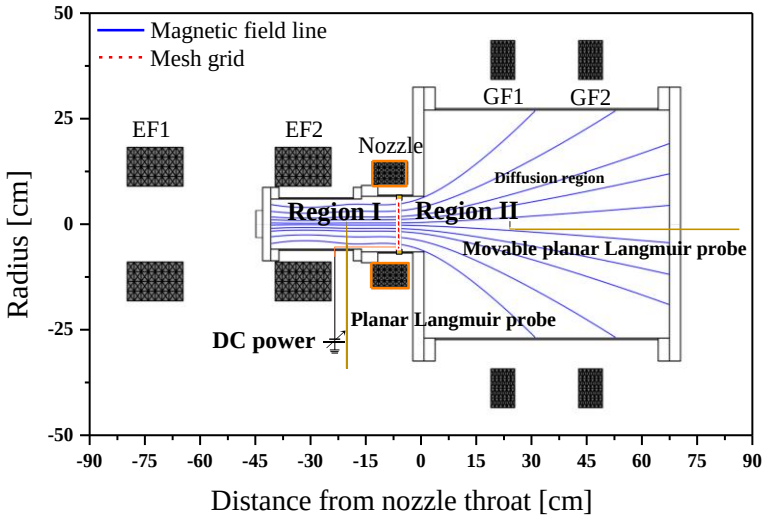

Figure 2.2. Schematic diagram of the ECR MN showing the divergent magnetic field configuration with mesh grid and two Langmuir probes. The mesh grid with line spacing of 1.68 mm (12 line per inch) is mounted at -6 cm from the nozzle throat to avoid ionization during the magnetic expansion.

2.1.2. ICP Magnetic Nozzle

The S-Nozzle device and magnetic field structure used in this study consists of three main components [Figs. 2.3(a) and (b)]; an electrically floated plasma source tube made of quartz wound with a silver-plated 2-turn cylindrical antenna; a grounded expansion chamber; a mesh grid (60 line per inch; grid line spacing of 0.25 mm) installed between the source tube and the expansion chamber [Fig. 2.4(a)]. The mesh grid is capable of applying pulsed voltage signal to determine the plasma properties just ahead the expansion region. RF powers (13.56 MHz) of 180 W connected to the L-type impedance matching circuit is applied to the antenna, and the reflected power under 1% is sustained during the experiment. A square wave changing from -90 V to 0 V (200 μs for -90 V and 400 μs for 0 V) is applied to the mesh grid through a signal generator [Fig. 2.4(b)]. The signal generator with an extremely fast rise time (4 ns) is used to prevent expansion of the ejected plasma from the mesh grid during the rise time of the pulsed signal. The two different regions (the source tube and expansion chamber) are separated by the nozzle field magnet to form converging-diverging magnetic field configuration [Fig. 2.3(a)].

A vacuum pumping system consists of an oil-sealed rotary pump (350 L/min) and a turbo molecular pump (1000 L/s). Using a mass flow controller with a maximum flow-rate of 100 mL/min, argon gas is injected through a gas feeding port at a radial center of the quartz tube. The base pressure is 5.0×10^{-7} Torr and the operating argon pressure is fixed at 4.0×10^{-4} Torr. Change of the operating pressure is not observed when various voltages are applied to the mesh grid, confirming that the pressure change during the experiments is negligible.

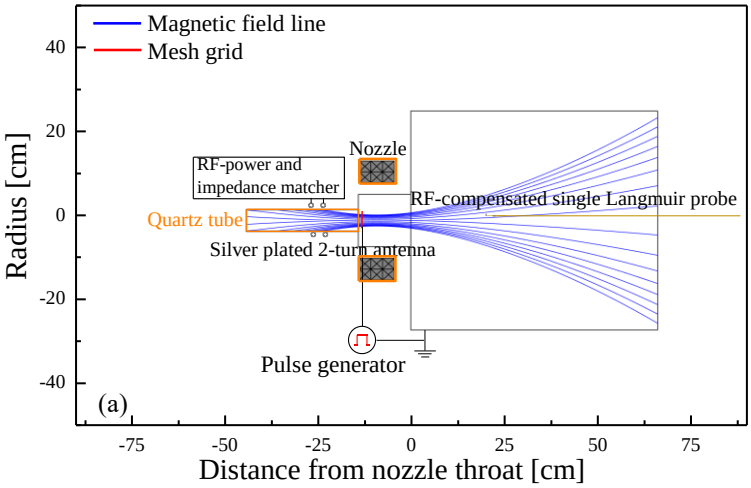

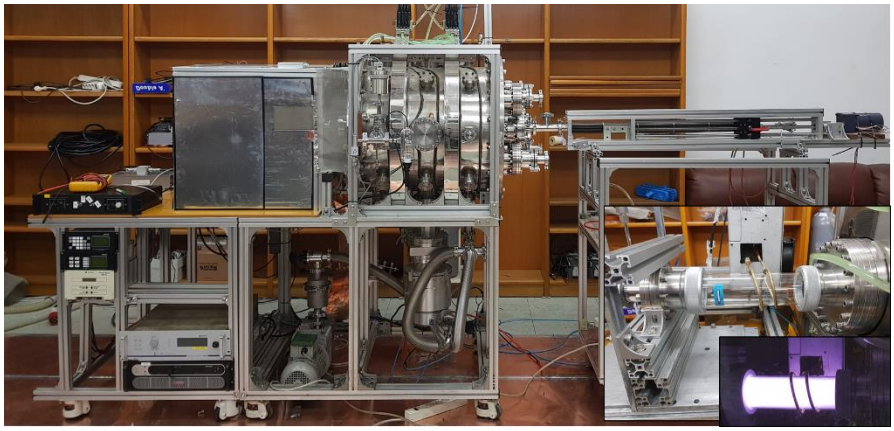

(b)

Figure 2.3. (a) Schematic diagram of the S-Nozzle device driven by the inductively coupled plasma source and the divergent magnetic field configuration. An axially movable RF-compensated single Langmuir probe is located at the expansion region and a mesh grid is installed at -13cm from the expansion chamber throat. (b) Photo of the S-Nozzle and inductively coupled plasma source. Cylindrical inductively coupled plasma source consists of an electrically floated plasma source tube made of quartz wound with a silver-plated 2-turn cylindrical antenna. Photo of plasma source during H-mode operation (an RF power of 180 W is applied to the antenna) is provided.

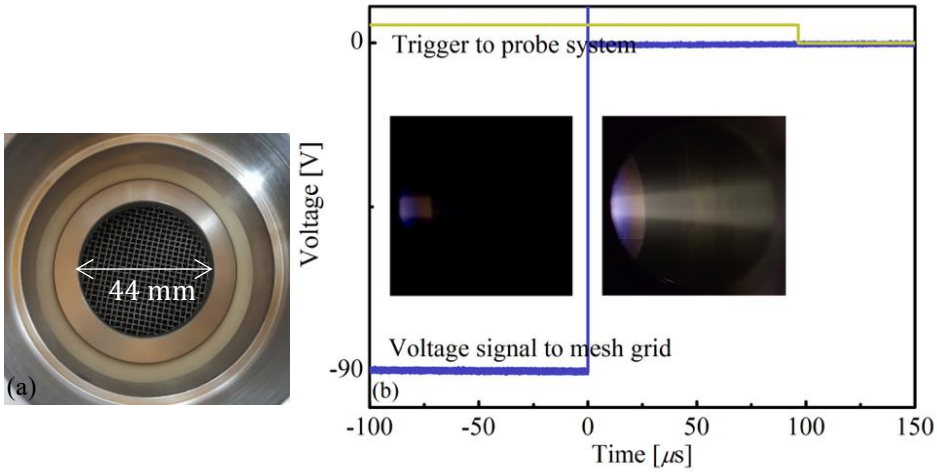

Figure 2.4. (a) Mounted mesh grid between the source tube and the expansion chamber; for electrical insulation with the chamber, a mesh grid set was fixed to the ceramic plate and connected to the chamber, and (b) the voltage signal to the mesh grid and trigger to probe system (the internal images, which were taken under the steady-state condition at each voltage, are inserted to aid the understanding of the experiment).

2.1.3. Main Assumption

This chapter describes the main assumptions used in this study, based on the calculated plasma parameters (e.g., length, and frequency scales) [Table 2]. In both the experiments (ECR and ICP MNs), the ionization degree defined as the ratio of the electron to neutral particle number densities is below 0.15%; thus, the long-range Coulomb collisions including electron-ion and electron-electron collisions can be neglected for weakly ionized plasmas. Rather, the collision process is dominated by short-range collisions between charged electron and neutral.

At the operating pressure, the calculated electron-neutral mean free path for the single-step ionization is much greater than chamber length at entire conditions. Relatively large collisional mean free paths compared to the expansion length scale ensure nearly collisionless plasmas. In addition, the bump structure is not observed in the high electron energy of the EEPFs; therefore, it is regarded that there is no or negligible electron beam suggesting that the electrons are created at the ECR zone in the source region and effects caused by the beam electrons via ionization and from the walls in the downstream region are negligible.

In magnetically expanding plasmas, the broken condition of the conservation of magnetic moment of particle can be expressed as $B_z/\nabla_{\parallel}B_z \ll v_{z,\alpha}/f_{c,\alpha}$, where $v_{z,\alpha}$, $f_{c,\alpha}$, and B_z are the particle velocity in z-direction, particle cyclotron frequency, and magnetic field strength along axial direction, respectively [27,47]. The subscript $\alpha = e, i$ denotes electrons and ions, respectively. This relationship indicates that the drift scale length of particles, $\mathrm{L}_{D,\alpha} = v_{z,\alpha}/f_{c,\alpha}$, during the characteristics scale length of the magnetic field inhomogeneity, $\mathrm{L}_B = B_z/\nabla_{\parallel}B_z$, can be dependent on the average particle velocity. In the case of the ECR MNs, the calculated degree of electron detachment $\mathrm{L}_{D,e}/\mathrm{L}_B$ at the nozzle throat is given as 2.7×10^{-4} for low B_z condition (nozzle current of 50 A) and 1.3×10^{-4} for high B_z condition (nozzle current of 200 A), respectively; however, that of the ions $\mathrm{L}_{D,i}/\mathrm{L}_B$ is 2.4 and 1.0 for both the cases, respectively. Since the ions obtain kinetic energy by self-generated electric field, the degree of ion detachment is increased along the divergent magnetic

field line. In the case of the ICP nozzle, $L_{D,e}/L_B$ and $L_{D,i}/L_B$ at the nozzle throat are 9.1×10^{-4} and 0.7, respectively. Therefore, it can be seen clearly that only the electrons are strongly tied to the magnetic field.

We shall assume a low-beta plasma

$$\beta \sim \mu_0 \frac{p_{e0}}{B_{Max}} \ll 1, \tag{2.1}$$

where μ_{e0}, p_{e0}, and B_{Max} are the magnetic moment, electron pressure, and magnetic field strength at the nozzle throat, respectively. This ensures that the plasma induced magnetic field can be neglected with respect to the applied magnetic field [46]. Therefore, the expansion in the MN devices can be regarded as collisionless, electron-magnetized, low-beta, and current-free jet.

Table 2. Main parameters at the nozzle throat based on data from experiments (0.1 eV of the temperature of Ar^+ is assumed). The low and high B-field condition in the ECR MN (microwave power of a 600 W) corresponds to 50 A and 200 A of the nozzle current, respectively.

Parameters at Nozzle Throat	ECR MN		ICP MN at $95\mu s$
	Low B-Field	High B-Field	
Argon Pressure [mTorr]	0.45		0.4
Ionization Degree [%]	0.15	0.07	0.005
Magnetic Field [G]	187	435	66
Electron Density [$\times 10^{10}$ cm^{-3}]	2.3	1.1	0.06
Electron Temperature [eV]	7.3	9.3	10
Electron Larmor Radius [cm]	0.05	0.04	0.16
Ion Larmor Radius [cm]	1.5	0.7	4.4
$L_{D,e}/L_B$	2.7×10^{-4}	1.3×10^{-4}	9.1×10^{-4}
$L_{D,i}/L_B$	2.4	1.0	6.7
Electron Mean Free Path / Diffusion Chamber length	1.7	1.7	1.9
Plasma Beta	2.0×10^{-4}	2.2×10^{-5}	6.0×10^{-5}
Frequencies [s^{-1}]			
Electron Cyclotron Frequency	5.2×10^{8}	1.2×10^{9}	1.9×10^{8}
Ion Cyclotron Frequency	7.1×10^{3}	1.7×10^{4}	2.5×10^{3}
Electron Ionization Collision	1.1×10^{5}	1.9×10^{5}	2.0×10^{5}
Electron-neutral Collision	4.0×10^{6}	4.6×10^{6}	4.2×10^{6}
Electron-ion Collision	2.5×10^{3}	8.8×10^{3}	5.3×10^{2}
Electron-electron Collision	1.7×10^{3}	6.2×10^{3}	3.7×10^{2}
Electron Plasma frequency	2.2×10^{8}	1.5×10^{8}	3.5×10^{7}
Ion Plasma Frequency	8.0×10^{5}	5.4×10^{5}	1.3×10^{5}
Velocities [m/s]			
Ion Sound Velocity [m/s]	4.2×10^{3}	4.7×10^{3}	4.9×10^{3}
Alfvén velocity [m/s]	1.4×10^{6}	4.6×10^{6}	3.0×10^{6}

2.2. Diagnostics

2.2.1. Measurement of Electron Energy Distribution

For the diagnostics of the ECR MN plasmas without the mesh grid, an axially movable double-sided planar Langmuir probe (front and back probes mounted back to back with a ceramic insulator between them) is placed at the radial center of the plasma diffusion region where the magnetic field line is purely axial [Fig. 2.5(a)]. Two planar probe tips were constructed from thin tantalum plate (diameter 6.1 mm); the planar probe tip has a larger radius than the electron Larmor radius because of the need to recognize the planar probe tip as an infinite plate. The use of relatively large size of double-sided planar Langmuir probe may cause the shadow effect, which can create a downstream wake. Therefore, the probable effect of the wake plasma on the back-probe measurement should be considered. In our experiment, it is assumed that both the Debye length and the electron Larmor radius are much smaller than the typical cross-field dimension of the probe. The mean free path for electron-neutral collision, which can cause the cross-field diffusion from the wake, exceed 1 m at the operating argon pressure at the nozzle throat and small Larmor radius inhibits the electrons of the downstream wake from entering the edge-shielded probe. Thus, the electrons in the wake remain strongly magnetized and hardly diffuse into back probe; the vector components of the electrons constituting the 1-D EEPF measured by back probe will be anti-parallel to the magnetic field along with negligible components of electrons from the cross-field diffusion. The insulator thickness separating the two tips is 3 mm, which is much shorter than the characteristic length of the electron density and temperature variations [Fig. 2.5(a)]. To eliminate edge effects [48] caused by sheath expansion, which is bias-voltage dependent, the edges of the probe area are shielded using a ceramic (Al_2O_3) cover. On the assumption that anisotropic thermodynamics of electrons may affect the measurement, we obtain the 1-D EEPF parallel (downward EEPF measured by front probe) or anti-parallel (upward EEPF

measured by back probe) to the magnetic field by taking the first derivative of the current–voltage curves measured with the double-sided planar Langmuir probe [49]. Then, the effective electron temperature corresponding to a mean electron energy is determined by $T_{eff} = 2/(3n_e)\int_0^\infty {\varepsilon_e}^{3/2} f_e(\varepsilon_e)\, d\varepsilon_e$, where ε_e is the electron kinetic energy, f_e is the EEPF, and n_e is the electron density, i.e., $n_e = \int_0^\infty {\varepsilon_e}^{1/2} f_e(\varepsilon_e)\, d\varepsilon_e$ [50,51]. The knee of the I–V curve is determined by the inflection point of the I–V characteristic curve (zero crossing of the second derivative) having a maximum uncertainty of 0.2%. For a planar Langmuir probe, the axial ion beam is directly collected by the probe tip and its effect can be reflected in the I-V characteristics as a second peak above the plasma potential. Therefore, the existence of the ion beam and its effect on the measured I-V characteristics were verified with an retarding field energy analyzer (RFEA) mounted at the radial center of the plasma diffusion region. From the measurement, we can assert that the existence of an ion beam mainly affects the shape of electron current region with $V_{bias} > V_p$ in a measured I-V characteristic, where V_{bias} and V_p are probe bias voltage and a knee at a lower voltage regarded as electron saturation current, respectively. Relatively large collisional mean free paths compared to the expansion length scale ensure nearly collisionless plasmas, showing no bump structure in the high electron energy of the EEPFs; therefore, it is regarded that there is no or negligible electron beam suggesting that the electrons are created at the ECR zone in the source region and effects caused by the beam electrons via ionization and from the walls in the downstream region are negligible.

For the diagnostics of the mesh grid mounted ECR MN, a planar Langmuir probe is additionally placed at the radial and axial center of Region I [Fig. 2.2], where the magnetic field line is purely axial. A probe tip is constructed from thin tantalum plate (diameter 6.1 mm), and the current is collected on both sides of the tip [Fig. 2.5(b)]; the probe surface can be considered as an infinite plane sheath because the probe surface has a larger radius than the electron Larmor radius. The probe is shielded using a ceramic (Al_2O_3) cover to prevent edge effects due to sheath expansion. The EEPFs

are obtained by calculating the second derivative of the measured I-V characteristic $I_e''(\varepsilon_e)$ with the assumption of isotropic plasmas. The second derivative $I_e''(\varepsilon_e)$ is proportional to $f_e(\varepsilon_e)$ which is related to the electron energy distribution function (EEDF) $g_e(\varepsilon_e) = \varepsilon_e^{1/2} f_e(\varepsilon_e)$. The plasma potential V_p is determined by the zero crossing of $I_e''(\varepsilon_e)$. The electron density n_e and the effective electron temperature T_{eff} corresponding to the mean electron energy are determined from the integral of the EEDF in a given electron energy

For the diagnostics of the ICP MN plasmas, since the oscillations of the probe current can distort the I-V curves by contributing to collection of a time-averaged current, which does not represent the inherent plasma characteristics, an RF-compensated single Langmuir probe with a floating loop reference ring and two-stage LC resonance choke filter [51] ($100\ \mathrm{kOhm}$ at $13.56\ \mathrm{MHz}$ and $35\ \mathrm{kOhm}$ at that of the second harmonic to reduce the RF distortion) is placed at the axial center of the plasma expansion region, where the magnetic field line is purely axial [Fig. 2.5(c) and Figs. 2.6(a) and (b)]. Since the impedance of the probe in the RF plasmas is pre-dominated by the probe sheath capacitance, the floating loop reference ring is electrically connected to the probe tip via a blocking capacitor (100 pF) to increase the coupling between the probe and the RF plasma and reduce the probe sheath impedance, ensuring that most RF voltage drop occurs in the LC resonance choke filter. Finally, the distortion of the I-V curve due to RF voltage rectification in the probe sheath is reduced. Probe tip is constructed from tungsten wire ($0.05\ \mathrm{mm}$ in radius and $15\ \mathrm{mm}$ in length); the tip has a smaller radius than the electron Larmor radius. A box-car averaging mode, which gives time-resolved diagnostics of the plasma parameters is used. Trigger to probe system is synchronized with the voltage signal to mesh grid [Fig. 2.4(b)], then at each cycle of the trigger signal, only some of the probe bias voltage to be measured is applied to the probe. Thus, the box-car mode can acquire data points in each period of the voltage signal to the mesh grid and the procedure is repeated over time to obtain a complete I-V curve. For the assumption of collisionless sheath around the collecting probe, the Larmor radius of the electrons should be taken into account for design of a probe. In all experimental conditions, the

radius of the probe sheath is always shorter than the electron Larmor radius; thus, the EEPFs is obtained by calculating the second derivative of the measured I-V characteristic $I_{\mathrm{e}}''(\varepsilon)$ with the assumption of isotropic plasmas. Experiments were conducted after an hour of the chamber conditioning and repeatability of the experiment data was verified.

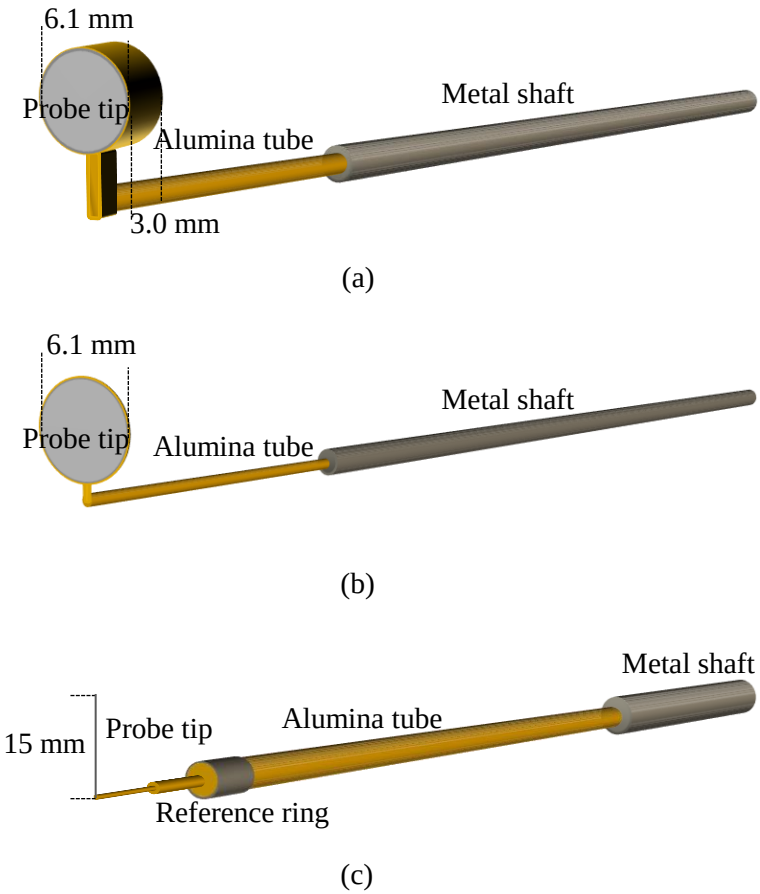

Figure 2.5. Schematic of the Langmuir probes; (a) a double-sided planar Langmuir probe. The front and back probe collects the plasmas in the direction toward the far-field and the nozzle-throat, respectively; (b) a planar Langmuir probe (both sides of the probe tip simultaneously collect the current signal from the plasma); (c) RF-compensated single Langmuir probe [51].

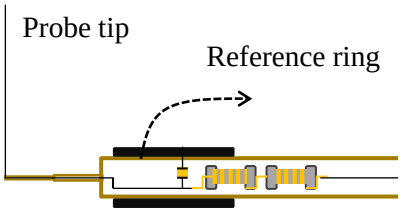

Blocking capacitor (ceramic chip; 100 pF) and two-stage choke filters (ferrite beads wounded with enameled copper wire)

(a)

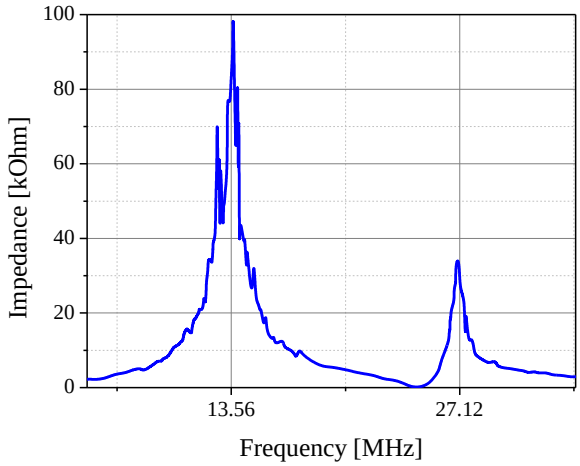

(b)

Figure 2.6. (a) RF compensation circuitry of a probe filter system with double-stage LC choke filter, reference ring, and blocking capacitor, and (b) S_{11} parameter of the single Langmuir probe measured through network analyzer.

2.2.2. Measurement of Ion Energy Distribution

An RFEA is used to measure the ion energy distribution of plasma and located at the expansion region of the ECR MN system, where the magnetic field line is purely axial [Figs. 2.7(a-c)]. The RFEA is constructed using four series of electrostatically biased mesh grids with a collector. The space between grids is shorter than $4\lambda_d$, where λ_d is the Debye length, to avoid build-up of charges and individual wires of mesh grid is closer together than λ_d to discriminate against to un-desired collection of particles.

All grids are placed in alignment inside an isolated case made of Al_2O_3, and the role of each grid is as follows; in the case of the earth grid located closest to the plasma, probable influences of electro-static field applied to the other electrodes are minimizes before the particles reach to the RFEA. The repellor grid is biased at a high negative potential to prevent the diffusion of the electrons while only the ions can pass through the mesh grid. Then, probe bias voltage to be measured is applied to the discriminator grid to obtain the I-V curve. The suppressor can repulse the secondary electrons generated by the ion bombardment and reduce the noise of the I-V curve. Finally, the ions with the energy range selected by the discriminator can be collected and the axial profile of the ion energy distribution function (IEDF) $f_i(\varepsilon_i)$ can be obtained through the first derivative of the I-V curve as follows; $dI_c/dV_d = Ae^2/m_i f_i(\varepsilon_i)$, where I_c, V_d, A, e, and m_i are the collector current, discriminator voltage, orifice surface area, elementary charge, and ion mass, respectively.

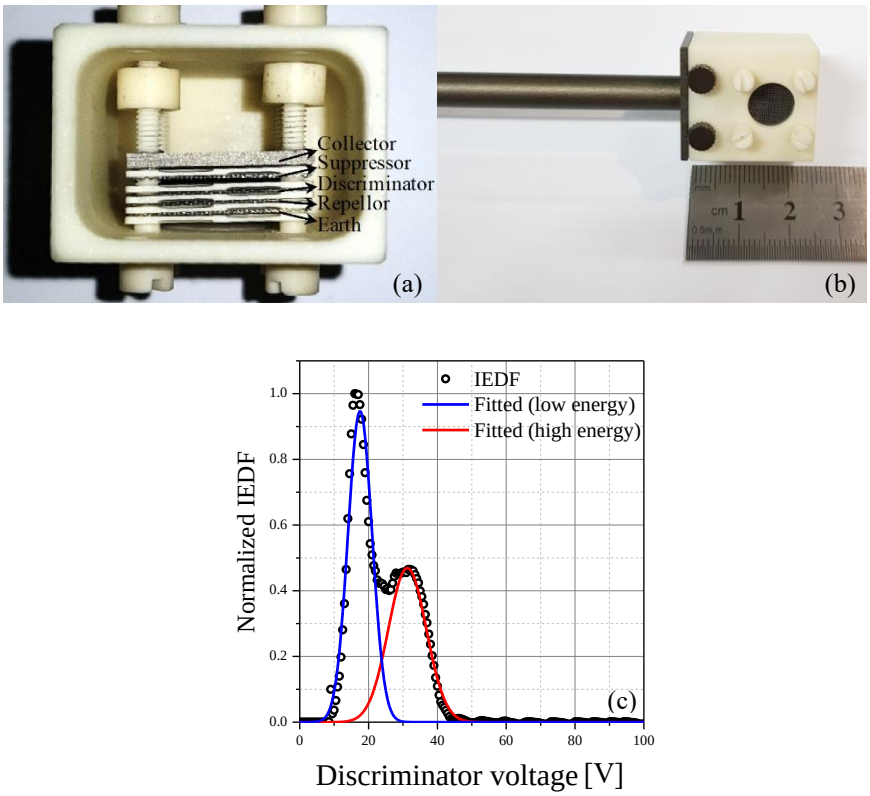

Figure 2.7. (a) Inside of an RFEA, (b) head of an RFEA; five wires are physically connected to each grid and are put through anodized shaft, and (c) an example of the IEDF fitted by Gaussian functions. The IEDF exhibits two peaks; the low energy component centers at the local plasma potential, and the beam energy is determined by subtracting the maximum value of the high energy component from the local plasma potential.

Chapter 3. Identification of Trapped Electrons with Steady-state Measurement

3.1. Measurement of 1-D EEPFs with Double-sided Langmuir Probe

From the measured downward and upward 1-D EEPFs [Figs. 3.1(a-d)] obtained at 2 cm intervals from 3 cm (the leftmost curve) to 49 cm (the rightmost curve) from the nozzle throat at two nozzle currents (50 A and 200 A), spatial evolution of EEPFs can be distinguished in each case. At low nozzle current [Figs. 3.1(a) and (c)], only the significant decrease in the electron density along axial direction is seen, and noticeable cooling of electrons are not observed in both probe measurements. Unlike the results at low nozzle current, the parallel anisotropy of the measured EEPFs represented as the discrepancy between the evolution of downward and upward EEPFs near the nozzle throat (Region I) is clearly seen at high nozzle current [Figs. 3.1(b) and (d)].

For the front probe [Fig. 3.1(b)] at high nozzle current, the measured EEPFs have an almost Maxwellian distribution and the cooling of electrons with distance from the nozzle throat (decay in the inverse slope of EEPF) occurs over the entire electron energy range. In contrast, the EEPFs measured by the back probe [Fig. 3.1(d)] are distinctly non-Maxwellian distributions and do not show a significant variation in the slope. This distinctive feature of the EEPFs between the downward and upward direction implies that at least two electron groups having different thermodynamic properties coexist near the nozzle throat.

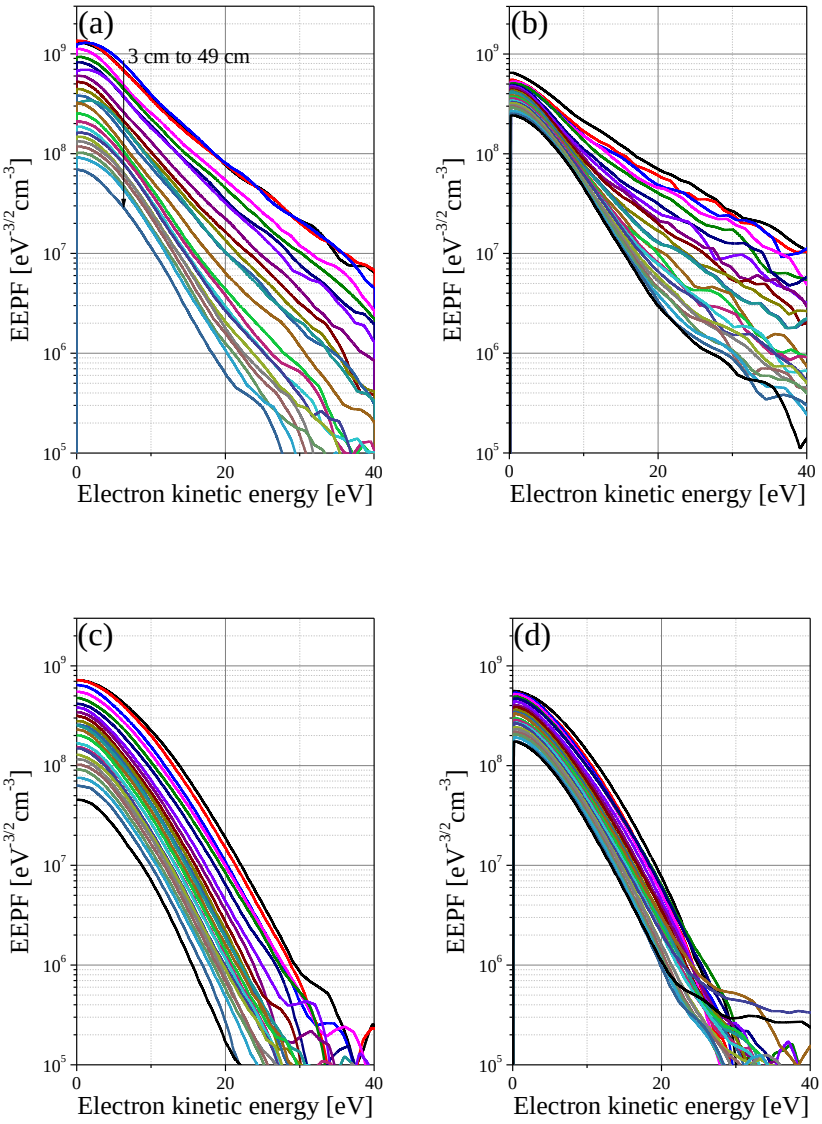

Figure 3.1. Axial variation of EEPFs in electron kinetic energy scale measured by (a) front and (c) back probe at low nozzle current (50 A) and (b) front and (d) back probe at high nozzle current (200 A) at 2 cm intervals from 3 cm (leftmost curve) to 49 cm (rightmost curve) from the nozzle throat.

The shape of the upward EEPFs at two nozzle currents [Figs. 3.1(c) and (d)] resembles a high-energy-depleted convex distribution, which was already reported by Zhang et al. [41] for the helicon plasma operating at nearly collisionless plasma. The shape of the EEPFs is nearly constant with distance from the nozzle throat, except for the cut-off at low energy electrons corresponding to the plasma potential. Hence, the electrons measured by the back probe can be regarded as total-energy-conserving electrons obeying non- local kinetics.

In contrast to the upward EEPFs, the downward EEPFs near the nozzle throat obey nearly the Maxwellian distribution (strictly, at low magnetic field condition, accumulation of low energy electrons is observed) [Figs. 3.1(a) and (b)]. However, the shape of these EEPFs at high nozzle current [Fig. 3.1(b)] is greatly changed compared to that of low nozzle current with increasing distance from the nozzle throat, implying that the electrons collected by the front probe do not obey non-local kinetics. Hence, the spatial change in the inverse slope of the downward EEPFs, i.e., electron temperature, at high nozzle current results in an overall cooling of electrons ejected from the MN along the divergent magnetic field. Such a coexistence of two electron groups along parallel or anti-parallel direction to the magnetic field weaken [Figs. 3.1(b) and (d)] as the distance from the nozzle throat increases and completely disappears at the far-field region (Region II). As shown in Figs. 3.1(b) and (d), both the EEPFs measured by the front and back probes far from the nozzle throat are almost identical at all axial positions, except for the cut-off in low-energy electrons.

3.2. Axial Profile of Plasma Parameters

Axial variations of properties of the plasma, namely, effective electron temperature T_{eff} and electron density n_e show that the MN can be divided into two regions depending on the spatial variation of the measured plasma parameters [Figs. 3.2 and Figs 3.3]. In Region I at high nozzle current condition, T_{eff} measured by the front probe [Fig. 3.3(b)] decreases rapidly compare to that of low nozzle current [Fig. 3.2(b)], although its variation gradually declines with distance (Region II), being nearly constant in Region II. On the other hand, T_{eff} measured by the back probe (1-D upward EEPFs) is slightly decreases with distance from nozzle throat in Region I [Fig. 3.2(b) and Fig. 3.3(b)], showing less pronounced variation compared with that of front probe measurements. In Region II, the electron-cooling behavior as found in both probe data is almost identical at two nozzle currents, indicating near-isothermal characteristics. Interestingly, the result exhibits a rapid spatial change in n_e (at the nozzle throat) only at low current conditions [Fig. 3.2(c)].

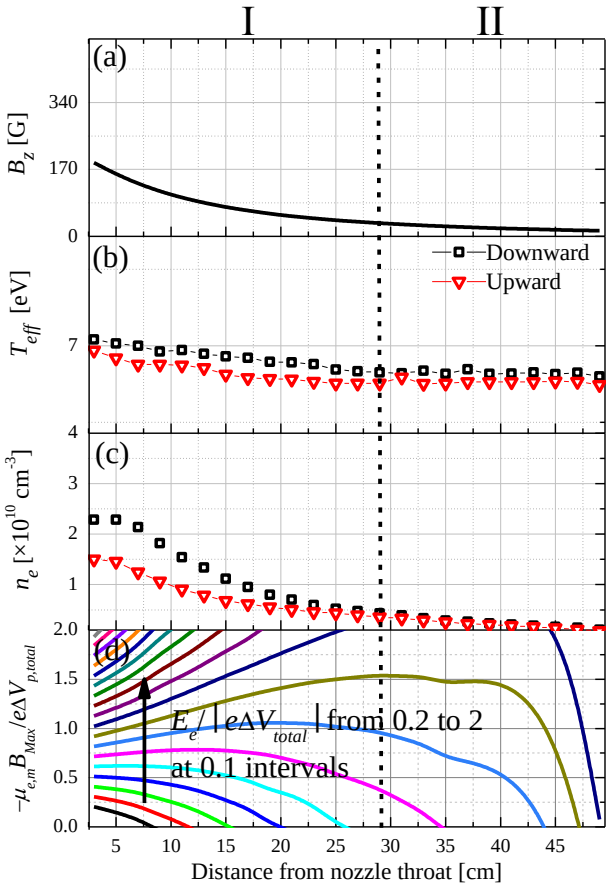

Figure 3.2. Axial profiles of electron parameters measured by front probe (open squares) and back probe (open triangles) from 3 cm to 49 cm from the nozzle throat at 50 A: axial magnetic field strength B_z, effective electron temperature T_{eff}, electron density n_e, and normalized maximum magnetic moment $-\mu_{e,m}B_{Max}/e\Delta V_{p,total}$.

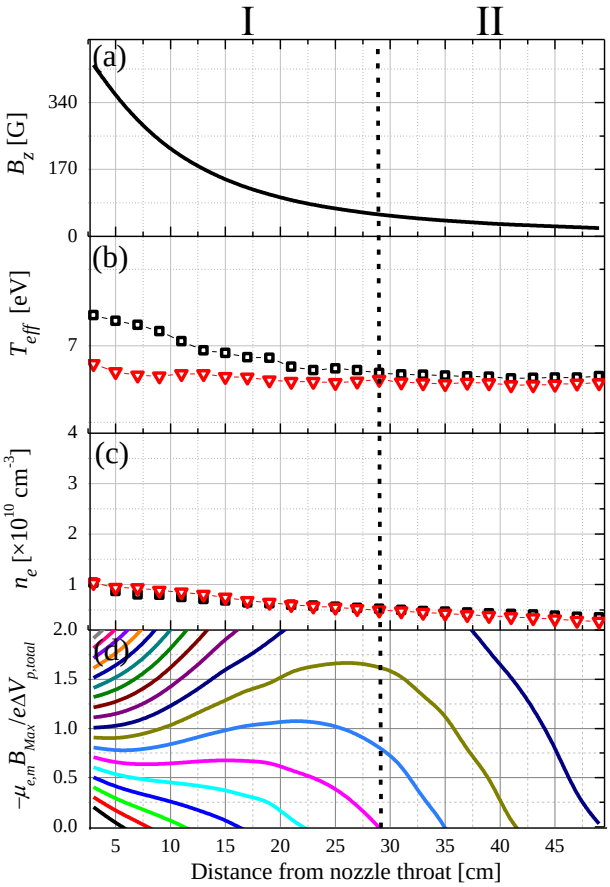

Figure 3.3. Axial profiles of electron parameters measured by front probe (open squares) and back probe (open triangles) from 3 cm to 49 cm from the nozzle throat at 200 A: axial magnetic field strength B_z, effective electron temperature T_{eff}, electron density n_e and normalized maximum magnetic moment $-\mu_{e,m}B_{Max}/e\Delta V_{p,total}$.

3.3. Thermodynamic Property of Electrons

From a fluids approach, expressions relating the variations in plasma properties along the divergent magnetic field obey electron thermodynamics, i.e., a polytropic equation. In general, a linear regression of the $log_{10} V_p$ vs log_{10} or V_p vs T_e data has been used to extract a value for γ_e [15,41-44,52,58]. The previous studies assume the Maxwellian distribution of electrons and combine the correlation between the electron pressure and the electric field with the polytropic equation through the electron momentum equation. However, the non-Maxwellian distribution typically observed under collisionless conditions requires a kinetic approach. From a kinetics perspective, the effective electron pressure and electron density can be directly calculated using the measured 1-D EEPFs. A polytropic equation [Eq. (1.4)] can be easily evaluated from

$$\log \int_0^\infty {\varepsilon_e}^{3/2} f(\varepsilon_e)\, d\varepsilon_e \propto \gamma_e \log \int_0^\infty {\varepsilon_e}^{\frac{1}{2}} f(\varepsilon_e)\, d\varepsilon_e. \tag{3.1}$$

The dynamics of the electrons, which are measured by the front probe near the nozzle throat at 200 A, follows a polytropic law with index $\gamma_e = 1.68 \pm 0.02$ (3σ) in Region I obtained using the linear regression method [Fig. 3.4(b)]. In Region II, at high nozzle current [Fig. 3.4(b)], p_e continuously decreases with rarely changing downward T_{eff} and eventually manifesting isothermal behavior with $\gamma_e = 1.10 \pm 0.01$ (3σ). In contrast, no significant variation in slope is observed with the upward electrons at high nozzle current [Fig. 3.4(b)]; the data show a slightly high γ_e than unity, $\gamma_e = 1.14 \pm 0.01$ (3σ) and $\gamma_e = 1.03 \pm 0.01$ (3σ) in Regions I and II, respectively. At low MN current (50 A), the measured γ_e averaged over both the 1-D downward and upward EEPFs shows nearly isothermal value in the entire region [Fig. 3.4(a)]. The results shown here indicate that the selectively collected electrons moving upward by back probe, which are regarded as trapped electrons, behave nearly isothermally in the MN even though the magnetic field strength varies.

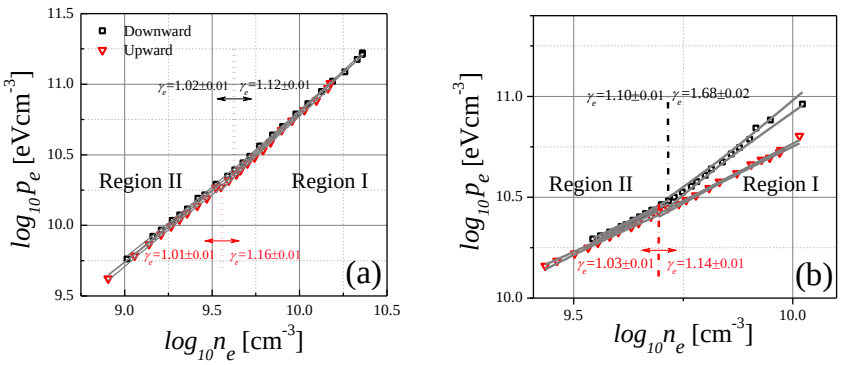

Figure 3.4. Log–log relationship between the effective electron pressure p_e and the electron density n_e averaged over 1-D EEPFs obtained at 2 cm intervals from 3 cm to 49 cm from the nozzle throat. The relationship indicates that the polytropic index of the MN system is determined by a combination of thermodynamic properties of each electron group, showing (a) the nearly isothermal behavior at 50 A, and (b) the coexistence of adiabatic and isothermal groups near the nozzle throat and its evolution into the isothermal at the far-field region at 200 A. The upper and lower limit curves from the 3σ rule are drawn as solid lines.

To clearly observe the spatial change in downward γ_e, we conducted the experiment by varying the applied magnet current. In contrast to previous study [41], the convex-shape EEPFs were not observed under all experimental conditions at the nozzle throat with a front probe, and the correlation between the strength of the applied magnetic field and γ_e is clearly observed. As the MN current decreases the isothermal region is expanded to the nozzle throat and γ_e averaging the 1-D downward EEPFs measured over the entire region of the MN evolves into isothermal [Figs. 3.5(a-d)].

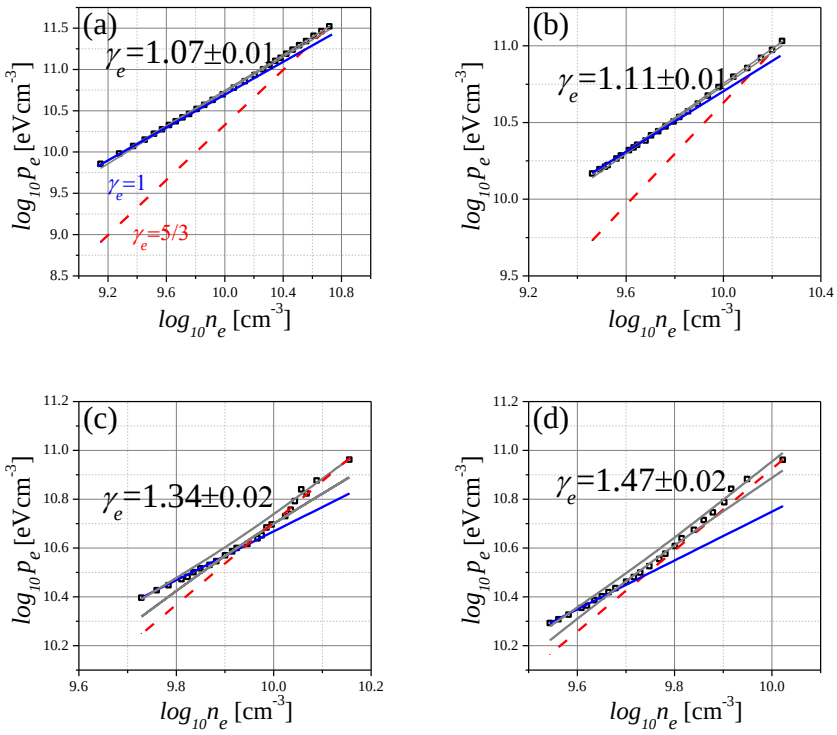

Figure 3.5. Dependency of γ_e on the strength of the applied magnetic field. The polytropic index determined by log–log relationship between the effective electron pressure p_e and the electron density n_e averaged over downward EEPFs by the upper and lower limit curves from the 3σ rule drawn as solid lines without dividing the nozzle area at (a) 50 A, (b) 100 A, (c) 150 A, and (d) 200 A, respectively. Polytropic curves with an index of 5/3 (dashed red) and unity (solid blue) representing the adiabatic and isothermal process, respectively.

3.4. Correlation Between the Bounce Region of Trapped Electrons and Local Maximum Magnetic Moment

The change in γ_e presenting the expansion of isothermal region from the far-field region can be explained by dividing electrons into adiabatic and isothermal groups. The downward electrons measured by the front probe near the nozzle throat at high nozzle current can be regarded as adiabatic electrons according to their motion observed in the spatial evolution of γ_e. The electrons responsible for the adiabatic expansion produce spatial changes in the slope of the downward 1-D EEPFs along the axial direction, relating γ_e closer to 5/3 near the nozzle throat. In comparison to the adiabatic electrons, the newly observed electrons measured by the back probe, which cannot be explained by adiabatic cooling, can be classified into groups of free and trapped electrons according to their energy and magnetic moment values [35].

When a particle is present in the divergent magnetic field, the total energy E_α and magnetic moment of the particle μ_α can be expressed as follow;

$$E_\alpha = \frac{m_\alpha}{2}\left(v_{\parallel,\alpha}^2 + v_{\perp,\alpha}^2\right) \pm e\Delta V_p, \tag{3.2}$$

$$\mu_\alpha = \frac{m_\alpha v_{\perp,\alpha}^2}{2B_z}, \tag{3.3}$$

where $v_{\parallel,\alpha}$ and $v_{\perp,\alpha}$ are the velocity components of a particle parallel and perpendicular to the magnetic field line, respectively, and m_α is particle mass. Since we are interested in the electrons with thermal energy conserved behavior, we can arrange above equations in terms of the invariants of motion;

$$v_{\parallel,e} = \pm\sqrt{\frac{2}{m_e}\left[E_e + e\Delta V_p - \mu_e B_z\right]}. \tag{3.4}$$

Thus, the electrons with $E_e + e\Delta V_p - \mu_e B_z > 0$ can drift in either direction along electric and magnetic fields, and they must reverse direction at $v_{\parallel,e} = 0$ similar to magnetic mirror (they cannot have imaginary velocity). Thus, the axial motion of electrons is determined by two fields (i.e., magnetic field and self-generated electric field); considering only 1-D motion along the axial direction, the axial magnetic field accelerates electrons via the magnetic moment conservation; however, the self-

generated electric field interferes with the magnetic expansion into the downstream region. Therefore, the position where electrons are present according to the total energy of electrons is determined by the combination of the magnetic mirror and the electric field. From this perspective, the local maximum magnetic moment $\mu_{e,m}$ with total energy E_e can be expressed as follows: $\mu_{e,m} = \left(E_e + e\Delta V_p\right)/B_z$; this point acts as the electron bounce location.

Therefore, the electrons emitted from the source exit can be classified into three groups. When the electrons having E_e higher than the total potential drop $\left|e\Delta V_{p,total}\right|$ along the axial direction in the diffusion region, the electrons ejected from the source region can freely escape to the wall without bounce motion [Fig. 3.6(a)]. The electrons with $E_e < \left|e\Delta V_{p,total}\right|$ emitted at the source exit will be reflected or double-trapped when they reach the barrier of the maximum magnetic moment in the downstream region. Assuming that the electrons have cooled through adiabatic process (which is the same situation as low energy electrons are incident on virtual region of the expansion region), the behavior of electrons unconnected to the source region with $E_e < \left|e\Delta V_{p,total}\right|$ can be trapped in the maximum magnetic moment well; the local maximum magnetic moment can have minimum and maximum values at points [Fig. 3.6(b)], which eventually manifests the bounce motion in a MN. Therefore, the trapped electrons having energy below the total potential drop then bounce back (reflected and trapped electrons) and forward (trapped electrons) in the effective potential well.

Normalized $\mu_{e,m}$ by $\left|e\Delta V_{p,total}\right|$ and the maximum magnetic field strength at the nozzle throat B_{Max} shows that the bounce region (i.e., effective potential well), where the electrons are trapped, expands to the nozzle throat as the magnetic field is weaken [Fig. 3.2(d), Fig. 3.3(d), and Fig. 3.7]; thus, the proportion of the isothermally behaving trapped electrons significantly increases at the nozzle throat as the MN current decreases, which results in the overall decrease of the measured γ_e averaged over 1-D downward EEPFs even at the nozzle throat [Fig. 3.4(a)].

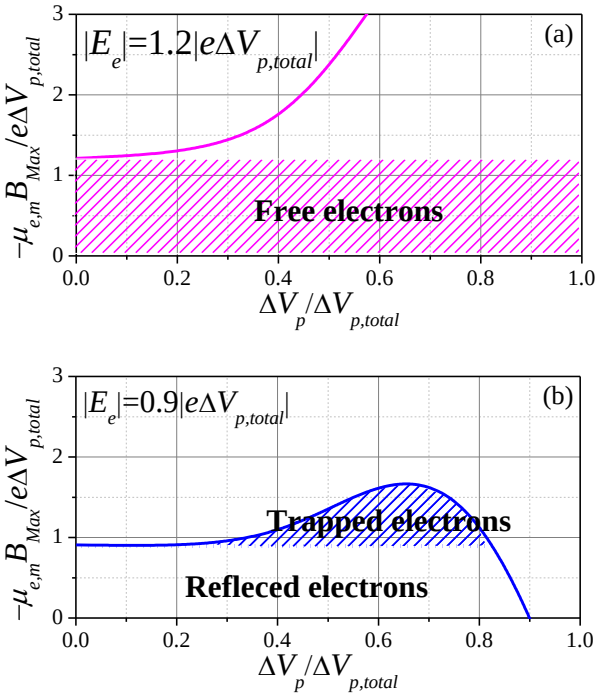

Figure 3.6. Example of the normalized local maximum magnetic moment $-\mu_{e,m}B_{Max}/e\Delta V_{p,total}$ versus normalized potential drop $\Delta V_p\ /\Delta V_{p,total}$ for electron energy E_e of (a) $1.2\left|e\Delta V_{p,total}\right|$, and (b) $0.9\left|e\Delta V_{p,total}\right|$ for arbitral structure of the electric and magnetic fields.

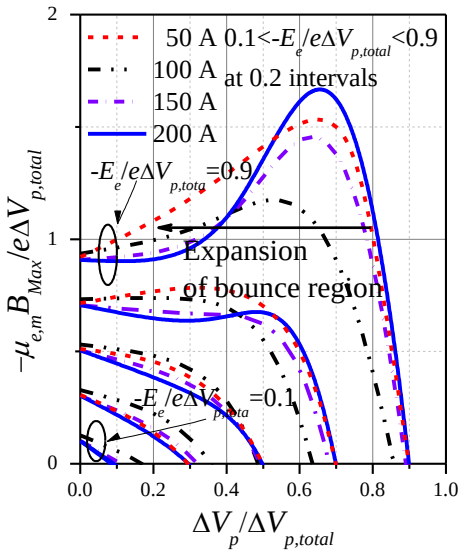

Figure 3.7. The figure shows the normalized local maximum magnetic moment $-\mu_{e,m}B_{Max}/e\Delta V_{p,total}$ versus normalized potential drop $\Delta V_p\ /\Delta V_{p,total}$ for various normalized electron energies $-E_e/e\Delta V_{p,total}$at nozzle current increasing from 50 A to 200 A.

3.5. Influence of Trapped Electrons on Electron Energy Distribution

As the transition of electron thermodynamic occurs from nearly adiabatic to isothermal, the EEPFs measured at the nozzle throat show abrupt increase of low energy electrons, whereas the significant change in the EEPFs slope is not observed at high energy range [Fig. 3.8(a)]; as the magnetic field strength is reduced, the collision frequency among electrons at the nozzle throat is increased about 3.6 times [Table. 2]. The results of this experiment showing the opposite trend with respect to a typical low-pressure discharge, at which the thermalization of the electrons (Maxwellianization) occurs with increasing the electron density due to increased electron-electron collisions, can be correlated to the existence of non-locally behaving trapped electrons.

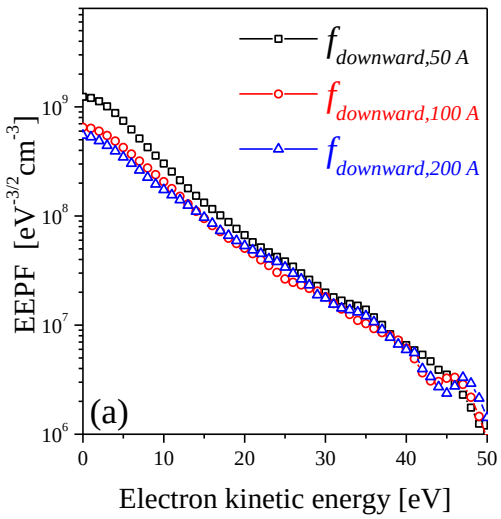
$f_{downward,50\ A}$
$f_{downward,100\ A}$
$f_{downward,200\ A}$
EEPF [eV$^{-3/2}$cm^{-3}]
(a)
Electron kinetic energy [eV]

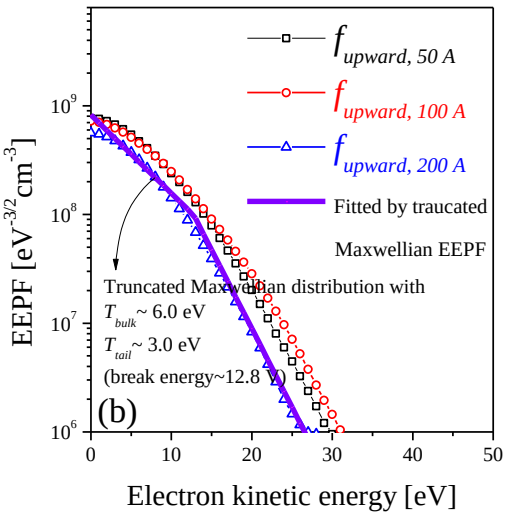
$f_{upward,\ 50\ A}$
$f_{upward,\ 100\ A}$
$f_{upward,\ 200\ A}$
Fitted by traucated
Maxwellian EEPF
Truncated Maxwellian distribution with
T_{bulk}~ 6.0 eV
T_{tail}~ 3.0 eV
(break energy~12.8 eV)
EEPF [eV$^{-3/2}$cm^{-3}]
(b)
Electron kinetic energy [eV]

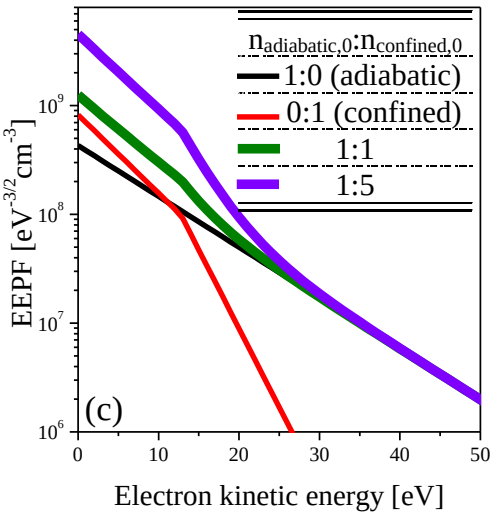

Figure 3.8. (a) The evolution of downward EEPF at the nozzle throat from the Maxwellian to non-Maxwellian distribution with increased proportion of low-energy electrons during the transition of electron thermodynamic from nearly adiabatic (200 A) to isothermal expansion (50 A), and (b) the measured upward EEPFs at the nozzle throat according to the magnetic field strength and fitted truncated EEPFs. (c) As the proportion of the non-locally behaving EEPFs increases, the abundance of low energy electrons is observed in the calculated distribution.

In Secs. 3.3 and 3.4, we showed that the transition of electron thermodynamics is accompanied by the expansion of the bounce region of non-locally behaving trapped electrons with low kinetic energy; the bounce region of the trapped electrons is expanded to the nozzle throat at the isothermal condition. Therefore, it can be assumed that a number of electrons with low kinetic energy is superimposed on the adiabatically expanding Maxwellian EEPF during the transition from adiabatic to isothermal. This assumption is experimentally demonstrated by observing the expansion process of the plasma over time.

By adopting the experimentally measured T_{eff} at the nozzle throat and spatial profile of n_e with front probe at nearly adiabatic condition (200 A), the spatial variations of T_{eff} of adiabatic group can be estimated by the polytropic equation with the polytropic index $\gamma_e = 5/3$. In addition, the plasma potential structure can be calculated by electron momentum conservation equations $en_eE = -\nabla p_e$ as the balance between the effective electron pressure p_e and the electric field E to obtain the axial variation of plasma parameters of the trapped electrons from the non-locally behaving truncated Maxwellian EEPF. The EEPF shape of the non-locally behaving trapped electrons can be fitted to the truncated Maxwellian distribution with the bulk electron temperature T_{bulk} and the tail temperature T_{tail} as [53]

$$\begin{cases} f(\varepsilon_e) = 2n_e/\pi^{1/2}T_{bulk}^{3/2}exp\left(-\varepsilon_e/T_{bulk}\right), (\varepsilon_e < \varepsilon_{depleted}) \\ 2n_e/\pi^{1/2}T_{bulk}^{3/2}exp\left(-\varepsilon_e/T_{tail}\right)exp\left(-\varepsilon_{depleted}\left(1/T_{bulk} - 1/T_{tail}\right)\right), (\varepsilon_e > \varepsilon_{depleted}) \end{cases}. \quad (3.5)$$

The shape of EEPFs recorded in the back probe (the trapped electrons) at all MN conditions is almost identical [Fig. 3.8(b)]; thus, the measured EEPF of trapped group can be described with a good degree of accuracy with a discontinuity occurring at the measured ion beam energy level $\varepsilon_{depleted}$ ~12.8 eV and a tail temperature T_{tail}~3.0 eV [Fig. 3.8(b)]. The fitted bulk temperature T_{bulk}~6.0 eV is determined by the cooled T_{eff} of adiabatic electrons, which was calculated through the polytropic equation [Fig. 3.8(b)]. This assumption is consistent with the experimental result that T_{eff} of the adiabatic and the trapped groups becomes identical at the far-field region.

Similar to the bi-Maxwellianization during the transition of electron

thermodynamics to isothermal shown in the experiment, a change in the low energy range is also observed in the calculated EEPF as the ratio of trapped electrons increased, showing the evolution into a bi-Maxwellian distribution like shape [Fig 3.8(c)]. The shape of measured downward EEPF at the nozzle current of 50 A is nearly equal to the calculated EEPF at a ratio of 1:1 [Fig 3.8(c)]. It is also expected that when adiabatically behaving Maxwellian distribution is affected by the nozzle wall leading to EEPF depletion at high electron energy, then the total EEPF with the truncated Maxwellian EEPF can evolve into the Druyvesteyn-like distribution.

The plasma parameters of non-local truncated Maxwellian distribution for the trapped electrons at different potential locations are represented by the energy shifted distributions with the amplitude consistency. Finally, the total density and temperature weighted for each electron group is evaluated [Figs. 3.9(a-c)]. As the proportion of the trapped group increases, the spatial variation of the total electron density dramatically increases with total electron temperature changing toward isothermal, which can represent the results observed in the experiment [Fig. 3.2(c)]. Eventually, the polytropic equation shows significantly reduced γ_e [Fig. 3.9(c)] with abrupt changes in p_e with increasing the proportion of trapped electrons.

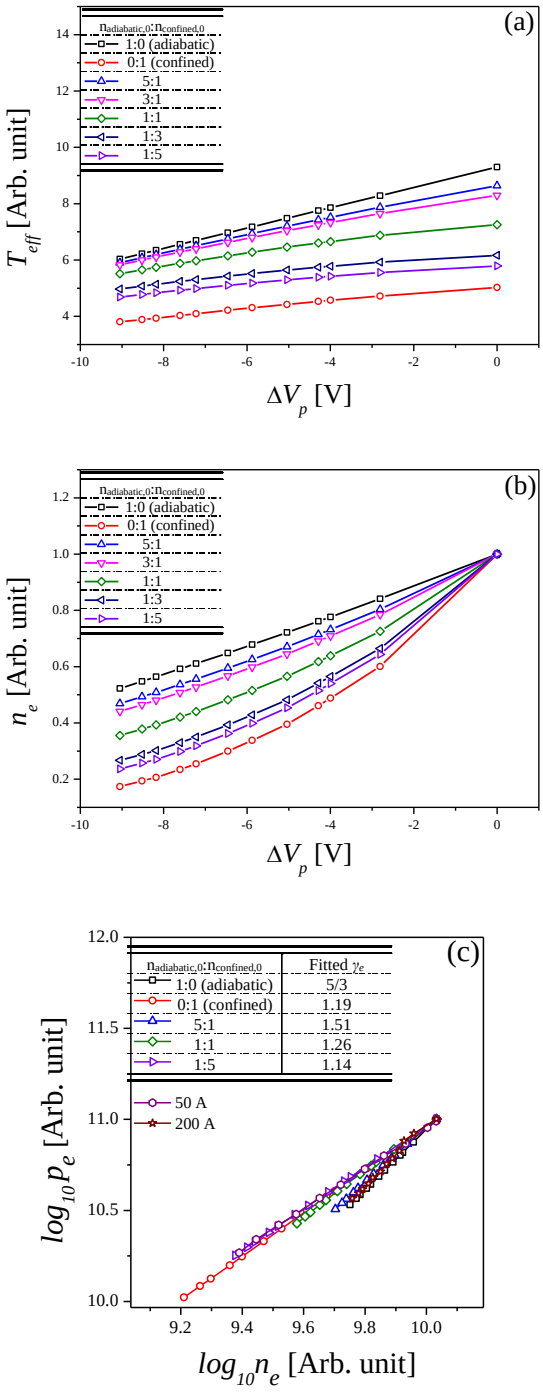

Figure 3.9. (a) Effective electron temperature, (b) electron density as a function of

plasma potential variation for various ratio of adiabatic electrons to non-locally behaving electrons, and (c) log–log relationship between the electron pressure p_e and the electron density n_e calculated by model and averaged over measured 1-D EEPFs obtained at 2 cm intervals from 3 cm to 25 cm from the nozzle throat.

The spatial evolution of the total EEPFs according to the proportion of the trapped electrons to the adiabatic electrons can be determined based on the calculated plasma parameters, i.e. calculated n_e, T_{eff}, and the plasma potential structure [Figs. 3.10(a) and (b)]. As the proportion of electrons with truncated EEPFs, which represents the distribution of isothermally behaving trapped electrons, is included in the modeling, the axial variation of the calculated EEPF is similar to that of low nozzle current [Fig. 3.10(a)]. The accumulation of thermal energy conserved electrons by magnetic moment well described above can explain the isothermal behavior of electrons observed is the MNs having double layer plasma potential structures. When the spatial gradient of the plasma potential structure is set high similar to the double layer structure with fixed $|e\Delta V_{p,total}|$, the bounce region of the magnetic moment well becomes close to the nozzle throat [Fig. 3.11(a) and (b)]; accordingly, the proportion of the trapped electrons is expected to be increased as the potential gradient becomes higher near the nozzle throat, implying the expansion of the isothermal region in the diffusion region with the evolution of the EEPFs.

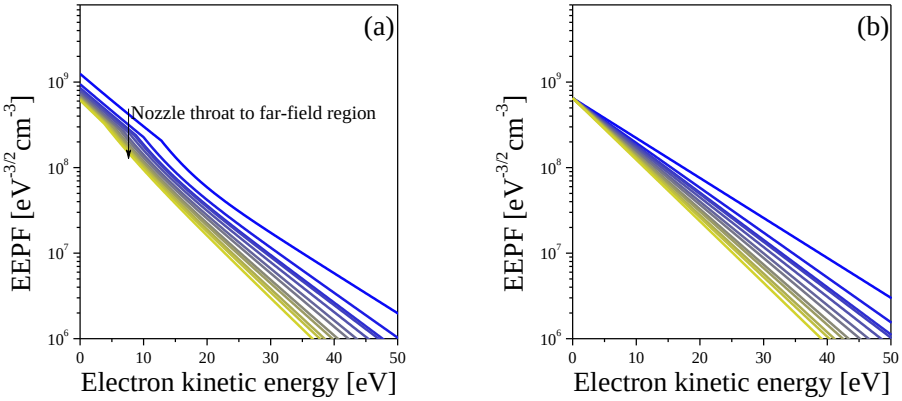

Figure 3.10. Calculated axial variation of EEPF at the density ratio of adiabatic to non-locally behaving electron: (a) 1:1, and (b) 1:0 (totally adiabatic electrons).

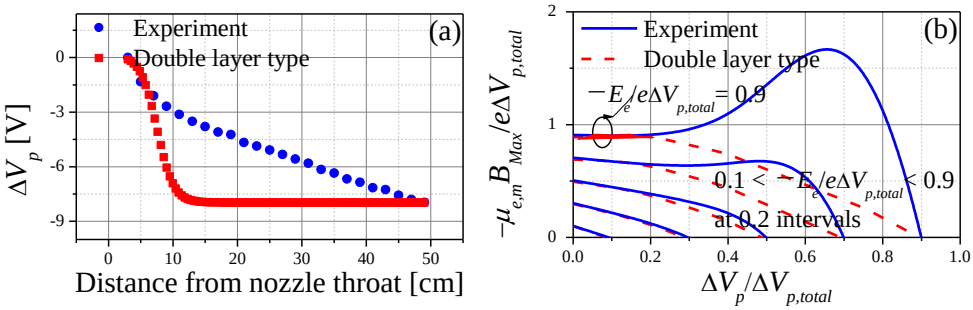

Figure 3.11. (a) Plasma potential structure at the nozzle current of 200 A and an arbitrarily generated structure to describe the double layer structure, and (b) $-\mu_{e,m}B_{Max}/e\Delta V_{p,total}$ versus normalized potential drop $\Delta V_p\ /\Delta V_{p,total}$ for various normalized electron energies $-E_e/e\Delta V_{p,total}$.

3.6. Influence of Trapped Electrons on Ion Acceleration

In the previous sections, we showed that the evaluated γ_e of a MN is affected by the existence of trapped electrons, showing change in γ_e which eventually deviates from 5/3 as the MN current decreases due to the expansion of bounce region in the potential well formed by external magnetic field and self-generating ambipolar potential. This finding arises an essential question whether isothermally behaving trapped electrons affect the ion acceleration which the fundamental function of the MN thruster is. To answer this question, detailed measurements of IEDFs are performed by axially movable RFEA to verify the correlation between the change of γ_e and the presence of ion beam over a wide range of MN current. Measurements are performed at the boundary of two regions (Region I and II) according to the transition of electron thermodynamics. Normalized IEDFs are found to have two peaks exhibiting the well-known high energy tail and can be fitted by two Gaussian functions, corresponding to the local plasma potential representing background ion group produced via a charge exchange process and the ion beam (high energy tail) resulting from the plasma potential structure. Although the mean free path of collision with neutral is shorter than the IEDF measurement position, it is expected that the effect on the deceleration will be very small [54]. Assuming that the MN consists of a mono-energetic ion beam, the average beam energy of the accelerated ions at each location (the central ~29 cm and far regions ~ 49 cm) can be estimated as 12.2 ± 0.7 V and 13.3 ± 0.4 V, respectively [Figs. 3.12(a) and (b)]. This result indicates that the plasma potential structure, which is directly related to the ion acceleration, is not affected by thermodynamic property of a MN influenced by isothermally behaving trapped electrons. To investigate the reliability of the measured IEDF showing two peaks, stretched structure of the magnetic field is generated by using additional electro-magnets located at the diffusion region. The measured axial profile of n_e and T_{eff} is nearly constant and the ion-beam (high energy tail in IEDFs) was not observed under the condition, which points out that the contribution of isothermal electrons on the ambipolar electric field is negligible. Therefore, ion acceleration should not be

directly inferred from the value of polytropic exponent γ_e because thermodynamic property of a MN is influenced by isothermally behaving trapped electrons as well as adiabatically expanding electrons.

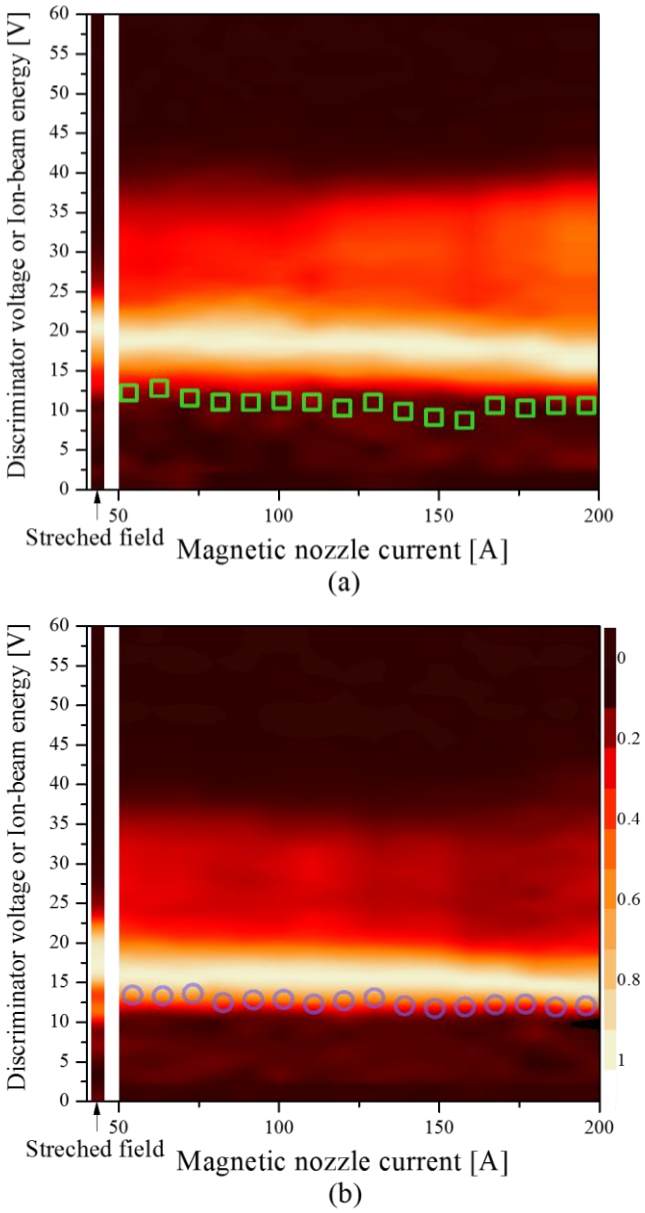

Figure 3.12. Normalized IEDFs (color bar) versus MN current obtained with RFEA at (a) 29 cm and (b) 49 cm from the nozzle throat. When the IEDFs can be fitted with two Gaussian ion populations (not provided here), the low energy and the high energy peaks correspond to the local plasma potential V_p and the beam potential V_{beam},

respectively. Therefore, the ion-beam energy ε_{beam} can be estimated as $\varepsilon_{beam} = e(V_p - V_{beam})$ and is plotted in (a) 29 cm, (green square) and (b) 49 cm, (blue circle), respectively. The IEDFs with stretched magnetic field structure do not show both the high energy tail and plasma potential variation, indicating there is no ion-beams in the entire region of the diffusion area.

3.7. Control of Electron Energy Distribution Through Mesh Grid in the ECR MN

In previous chapters, we observed the following peculiarity; the electrons are not considered to have typical characteristics as a single fluid due to not only the kinetic energy dependency on the particle behavior in the electric field and the magnetic field, but also the collisionless behavior of the electrons in a MN system leading to non-equilibrium state of the thermodynamic property. This feature is represented by the non-Maxwellian EEPF with low energy abundance observed at the low nozzle current conditions. Accordingly, it is not inappropriate to regard the magnetically expanding electrons as a single fluid and determine the representative value of the kinetic property; electrons can be grouped separately in one space assuming that the characteristics in the self-generated electric and magnetic field is determined by their kinetic energy. In the following chapters, we essentially grasp the origin of the two electron species observed in previous chapters (i.e., electron groups with adiabatic and isothermal behaviors). In order to accomplish this, it is essential to observe the progress of the effective potential structure over time; the logic give us an important assignment that the identification of which electrons contribute to the electric field formation is prioritized.

For the definite verification of how each group contributes to the formation of an electric field structure within in a magnetically expanding plasma, it is important to change the properties of plasmas at the source exit. Thus, it is examined whether the degree of the plasma diffusion from the plasma source region to the source exit is possibly controlled through the mesh grid in the ECR MN. The parameters that distinguish the two regions (i.e., plasma source and magnetically expanding region) of the ECR MN are designated as the DC voltage V_G applied to the mesh grid, and the axial profile of the plasma parameter is examined. Most importantly, we observe the changes in the plasma potential gradient as the electron properties in the diffusion region change; this study is a preliminary study to reveal dynamics of expansion and trapping of electrons during the build-up of the magnetic moment well structure in a

MN. At the end of this chapter, we propose a plasma device suitable for temporal observation of the plasma expansion.

Based on the point where the mesh grid is installed (-6 cm from the nozzle throat 0 cm), the ECR MN is divided into Region I and II. To precisely observe the plasma parameter dependence on V_G in Region I, a planar Langmuir probe is installed at the radial center of Region I at -15 cm away from the mesh grid. Although the measurement was not performed near the mesh grid, it is assumed that the variation of the plasma parameter along the magnetic field line in Region I is not large since the change in the intensity of the magnetic field in the axial direction is small. The plasma parameters show no significant change in Region I [Figs. 3.13(a-c)] according to V_G. That is, the electron property generated in Region II is achieved not by the changing the characteristics of the plasma in Region I but by the sheath generated in the grid installed between Region I and Region II. Then, newly appeared electron systems in the nozzle throat can expand to the diffusion region only by the magnetic field.

As V_G decreases the confinement effect of electrons becomes strong in Region I, and overall changes in the EEPFs in Region II represented as 1) the decrease in a slope of EEPFs and 2) the appearance of a high energy electrons with the shifted Maxwellian EEPF are observed. The principle that the source electrons get energy through the grid sheath, which is directly related to the formation of the high energy group, is as follows. The source electrons with energy higher than $\Delta V_{\mathrm{I}} = V_{p,\mathrm{I}} - V_G$ ($V_{p,\mathrm{I}}$ is the plasma potential at Region I) in Region I can overcome the grid sheath electric field and move forward to the axial center of the mesh grid (the diffused electrons lose their energy by ΔV_{I}) [Fig. 3.13(d)]. Then, the electrons are accelerated by the potential difference ΔV_{II} between V_G and V_p in Region II to have an energy shifted Maxwellian distribution [Fig. 3.13(e)]. As V_G decreases negatively, the threshold energy of electrons that can move from Region I to the axial grid center becomes higher, leading to the strong electron confinement in Region I. Accordingly, most electrons except the high energy electron group cannot pass through the mesh grid. As V_G decreases, the axial change in V_p gradually disappears, and at $V_G =$

-30 V, it is observed that the electric field in the bulk of Region II becomes very weak. In particular, axial variations of n_e and T_{eff} of the bulk group show the similar tendency as V_p [Figs. 3.14(a-d)]. The result suggests that electrons with sufficient thermal energy must be supplied to the nozzle throat in order to generate the potential gradient in the diffusion region; this corresponds to the electron enthalpy energy term in the evaluation of the thrust efficiency.

By reducing the thermal energy of electrons in the source exit via the EEPF control, overall decrease in the electric field is identified. The remained electron groups show thermal energy conserved properties during the reduction in the electric field, indicating that the electric field in the MN is created by the cooling of adiabatically expanding electrons and the rest groups having low thermal energy do not contribute in producing the electric field in the MN system. The temperature of high energy electrons is comparable to that of the thermal energy at $V_G = 0$ V, but they are observed not to contribute to the electric field formation; the mechanism for this requires further research.

Due to the nature of the ECR plasma source, the amount of high energy electrons in the source region is large, so that a great amount of high energy electrons is observed in the EEPFs during the electron filtering through the mesh grid. Their degree of coupling with the magnetic field can be defined independently of the bulk electron; thus, this phenomenon can serve as an unnecessary factor in a clear understanding of the observation of the plasma expansion process over time. Therefore, it is important to lower the proportion of the high energy electron at the source region to precisely understand the temporal evolution of the plasma parameters during expansion using the mesh grid.

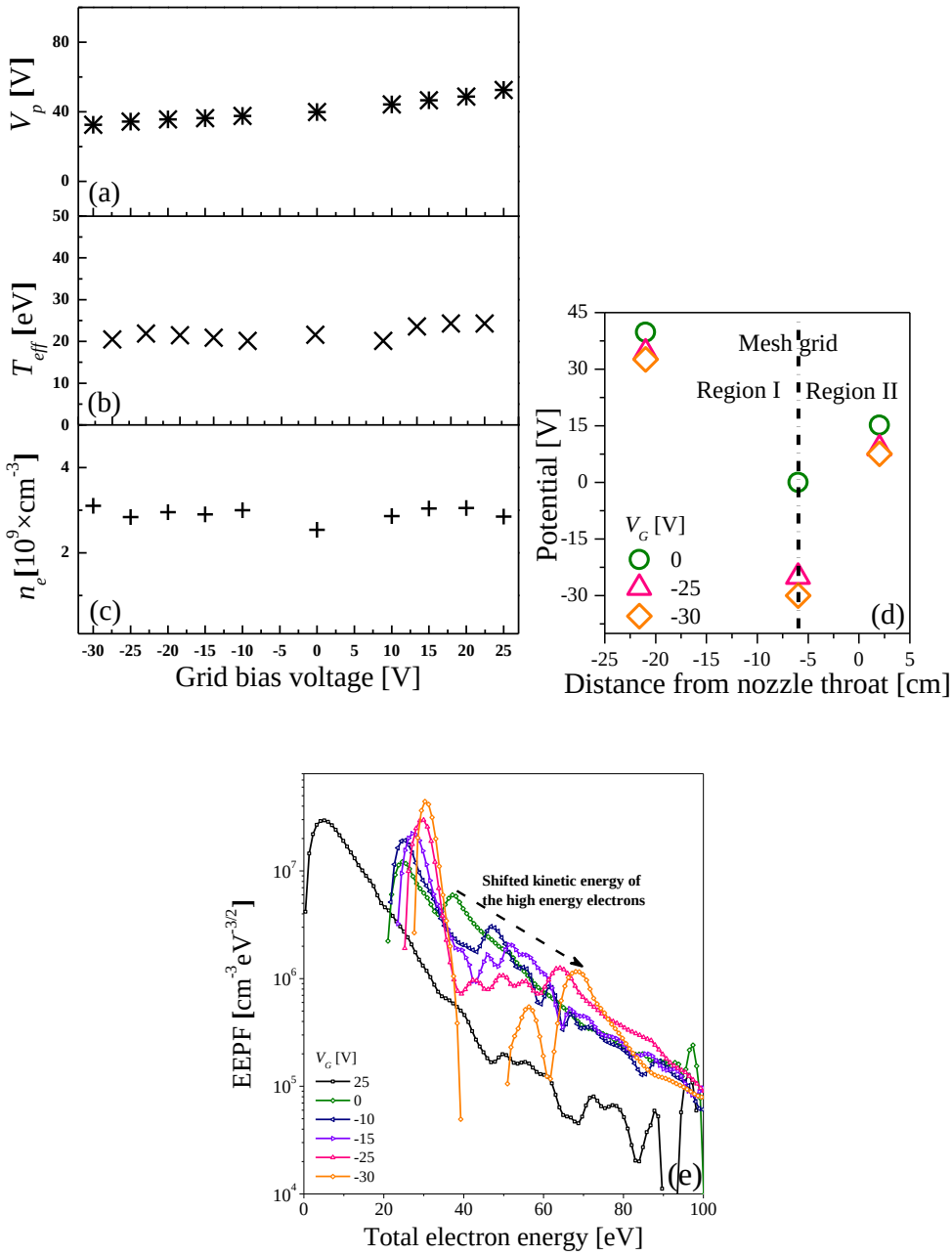

Figure 3.13. Variations of (a) V_p, (b) T_{eff}, (c) n_e measured at -21 cm from the nozzle throat (source region) according to mesh grid bias voltage V_G, (d) V_p in

Region I and II, and V_G, and (e) evolution of EEPFs according to V_G measured at $2\ \mathrm{cm}$ from the nozzle throat (Region II).

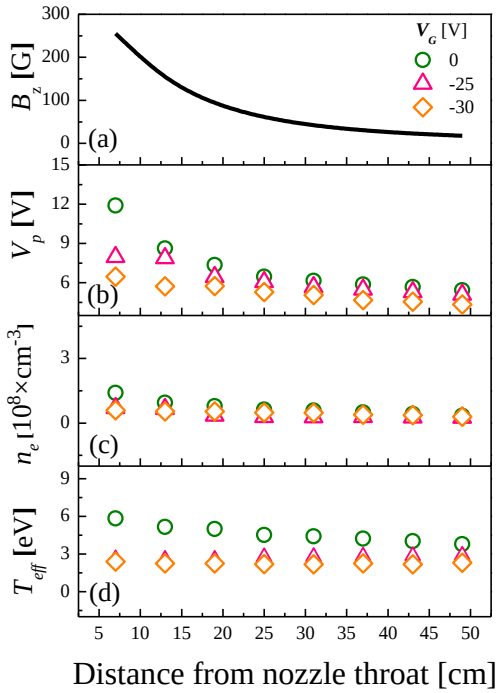

Figure 3.14. Axial profiles of (a) magnetic field strength B_z and (b) V_p, (c) n_e, and (d) T_{eff} according to mesh grid bias voltage V_G.

Chapter 4. Time-dependent Kinetic Analysis

4.1. Temporal Evolution of the Electron Energy Distribution

To solve the problem raised in previous chapter, an inductively coupled plasma (ICP) source is installed in order to minimize the high energy components in the source region; through the measurement of the EEPFs in the diffusion region, the high energy electrons are not observed in the entire experimental conditions, and time-dependent kinetic analysis can be achieved in the ICP MN device [58].

To see a series of the electron expansion process, temporal evolution of the EEPFs are measured at $2.0\ \mathrm{cm}$ intervals from $3\ \mathrm{cm}$ to $35\ \mathrm{cm}$ from the nozzle throat. The measured EEPFs do not show bump structure in the high energy tail, implying negligible electron beam components. When $-90\ \mathrm{V}$ is applied to the mesh grid ($0.5\ \mu\mathrm{s}$ before the rise up of the pulsed signal), confinement of the source plasma is strong that only a small amount of plasma can pass the mesh grid [Fig. 4.1(a)]. Accordingly, the plasma in the expansion region has relatively low n_e and T_{eff}, producing a negligible V_p structure in the expansion region [Figs. 4.1(b-d)].

The expansion of the source plasma into the low-density ambient plasma is achieved by pulsing the mesh grid to ground so that the confinement of source plasma is significantly reduced. Interestingly, as time elapsed, electrons begin to accumulate on the EEPFs [Figs. 4.1(b-e)]; the accumulation phenomenon increases with time over the entire expansion region. The accumulation of the electrons seen in the EEPFs directly attributes to n_e and T_{eff} changes over time ($3.0\ \mu\mathrm{s}$ to $95\ \mu\mathrm{s}$) throughout the entire expansion region [Fig. 4.2(c) and (d)]. Especially, at the initial stage ($3.0\ \mu\mathrm{s}$), the cooling of the electrons proceeds rapidly [Fig. 4.2(c)], and the absolute value of T_{eff} is reduced over time (the reduction near the nozzle throat is prominent). Unlike noteworthy changes in the absolute value of T_{eff}, the spatial

gradient of T_{eff} is appeared to be almost constant at each moment in the region closes to the nozzle throat. The spatial gradient of V_p tends to develop until $10\ \mu s$ [Fig. 4.2(b) and Fig 4.4(a)]. However, V_p gradient begins to be reduced after $10\ \mu s$ along with the reduced n_e profile in the downstream region, implying that the accumulated electrons in the downstream region at the later phase of the expansion contribute to reducing V_p structure. After all, only the trapped electrons with thermal energy conserved behavior can exist in the downstream, disconnected to the source region. The accumulated electrons begin to balance with existing electric field, and the plasma potential structure in the downstream follows electron density profile, showing reduced electric field.

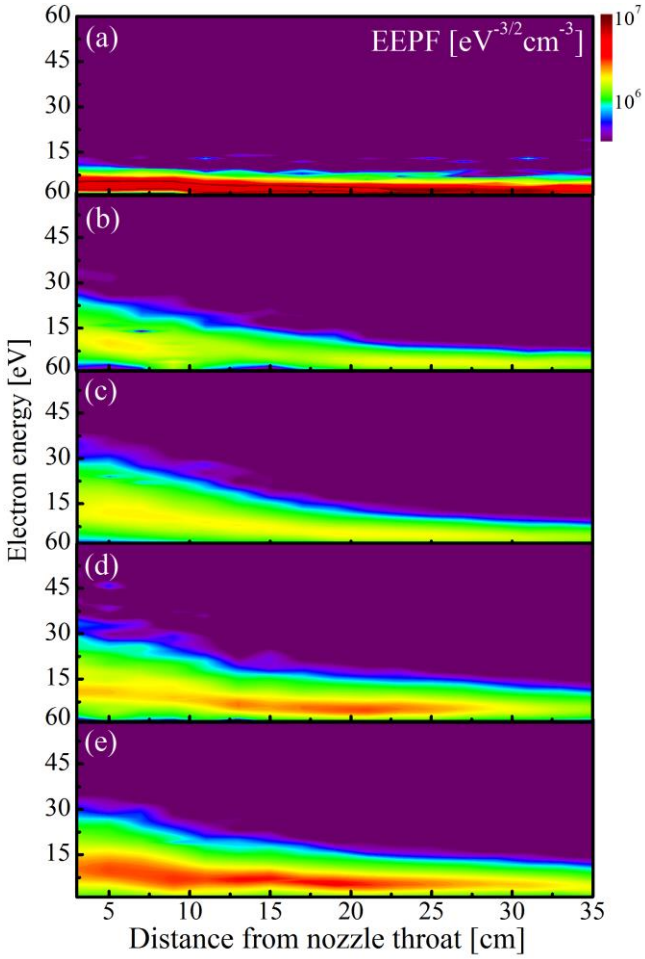

Figure 4.1. Time evolution of the EEPFs at (a) −0.5 μs, (b) 3.0 μs, (c) 7.5 μs, (d) 25 μs, and (e) 95 μs relative to the beginning of the pulse rise time (0 μs). In previous studies [55-57], time scale of plasma expansion into vacuum is close to an ion transit time due to the need of diffusion of the neutralizing ion from the source region to the expansion front at the initial stage of the expansion; however, in present study, the time scale of the expansion into the ambient plasma is rapid because such a neutralization ion can be provided by the ambient plasma.

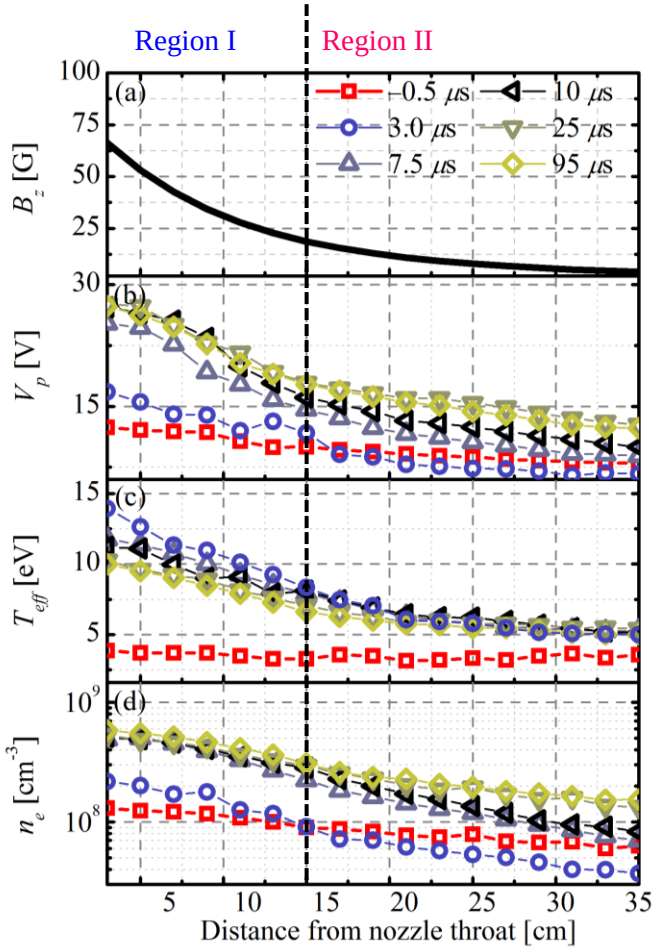

Figure 4.2. Axial profiles of (a) the magnetic field B_z and that of electron parameters from 3 cm to 35 cm from the nozzle throat over time: (b) V_p, (c) T_{eff}, and (d) n_e. All the plasma parameters were measured with an error range smaller than the size of the symbol (range of errors is below 5%).

4.2. Separation of the Expansion Region

In order to elaborate on the change of the EEPFs and plasma parameters, it is essential to consider the effective potential barrier which determines the electron motion in the MN. For electrons, the effective potential structure is determined by the local maximum magnetic moment $\mu_{e,m}$ with a total electron energy E_e as follows : $\mu_{e,m} = (E_e + e\Delta V_p)/B_z$. For simplicity, $\mu_{e,m}$ is normalized by the total potential drop along axial direction $\Delta V_{p,total}$ at each moment and the maximum magnetic field strength B_{Max}. The local maximum magnetic moment can have minimum and maximum values at certain locations past the nozzle throat, and this generates the well of the effective potential barrier, in which the electrons can be trapped.

When the electrons with $E_e = 20$ eV are located at the nozzle throat, the effective potential well (confinement region) is not generated at all moment (3.0 μs to 95 μs) [Figs. 4.3(b-d)]. In the case of relatively low energy electron (E_e of 12 eV and 16 eV), the well of the effective potential structure is formed in the expansion region, while the electrons at 3 μs can still escape freely to the far-field region without trapping [Fig. 4.3(b)]. Therefore, the behavior of electrons during the electric field formation in the expansion region can be described as follows; the electrons whose thermal energy is reduced through the adiabatic process are no longer involved in the cooling process and become disconnected to the source region by a build-up of maximum magnetic moment well. The formation of the confinement region shortens the magnetic expansion zone of the electron toward the nozzle throat. The initial electric field formation time ends at about 10 μs (ion plasma time scale is 15 μs; the time scale is obtained by the electron density at the nozzle throat at 3 μs). The time scale of the build of plasma potential structure is consistent with previous modeling works [62,63], in which the ion response time after fast electron expansion determines the electric field in the expansion region. During the formation of the electric field, the electrons collide with argon atoms via doubly trapped motion with the time scale of electron-atom collision period (0.3 μs) [61], leading to momentum

changes. After the initial electromagnetic field formation through adiabatic expansion and trapped motion in Region I and II, a transition to a new equilibrium state is observed in Region II separated from the source. The accumulation of the trapped electrons is accelerated in the downstream region as a second phase, and finally, the electric field in the downstream region disconnected to the source region is changed for $7\ \mu s$, which closes to ion plasma time scale, $10\ \mu s$, obtained by the electron density at $10\ \mu s$.

In previous studies regarding the time-resolved measurement of the plasma expansion into vacuum [55-57], the overall cooling of electrons by vacuum expansion is finished on the ion transit time scale (hundreds of μs). As a result, spatial cooling of electrons and generation of plasma potential gradient occur simultaneously; thus, it was not possible to observe spatial variation of plasma parameters due to electron trapping. In this study, after the rapid expansion of electrons along a divergent magnetic field to ambient plasma, the plasma potential is formed by the plasma frequency scale of the ions present. Therefore, it is meaningful that the magnetic mirror effect of electrons can be clarified by observing the accumulation of the trapped electrons on the initially generated plasma profile of cooled electrons. As a result, the characteristics of the accumulated electrons is superimposed on the initially generated axial profile of the plasma parameters. Eventually, the increased electron pressure due to the electrons with low thermal energy in the downstream region begins to balance with the existing V_p structure and eventually weaken the electric field in the region.

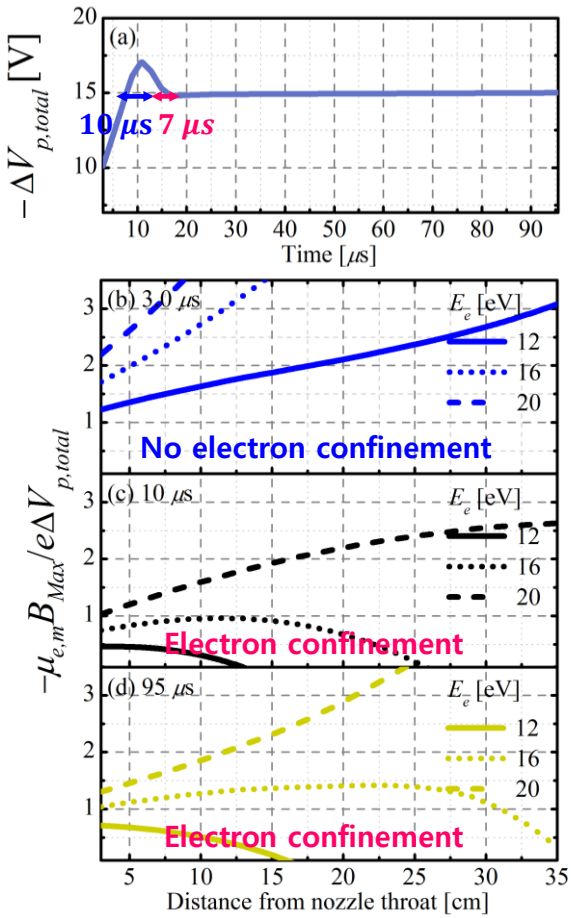

Figure 4.3. (a) Temporal variation of the total potential drop along axial direction $-\Delta V_{p,total}$, and the axial profiles of $-\mu_{e,m}B_{Max}/e\Delta V_{p,total}$ at (b) 3.0 μs,(c) 10 μs, and (d) 95 μs, respectively.

4.3. Time-dependent Kinetic Approach to Electron Thermodynamics

To clearly characterize the temporal evolution of these plasma parameters, we observe the electron thermodynamics by adopting the polytropic equation [58]. Previously, we mentioned that the effective electron pressure p_e and n_e for each electron group at certain moment can be related to the polytropic equation using the measured EEPFs; $log_{10}\int_0^\infty {\varepsilon_e}^{3/2} f_e(\varepsilon_e)\, d\varepsilon_e \propto \gamma_e log_{10}\int_0^\infty {\varepsilon_e}^{1/2} f_e(\varepsilon_e)\, d\varepsilon_e$. The *log-log* relationship of data shows that the adiabatic process dominates the electron thermodynamics near the nozzle throat at all moments [Fig. 4.4]. That is, the thermodynamic states of the electrons along the divergent magnetic field near the nozzle throat is maintained over time. Up to $3.0\,\mu s$, a slope of the *log-log* plot is maintained at the entire expansion region (the expansion seen in the downstream region far from the nozzle throat also follows the polytropic law with the exponent closes to the adiabatic process). In contrast, a temporal variation of the slope is observed beyond the central region. The evaluated γ_e becomes closer to unity as it approaches to the downstream (Region II), indicating that the electrons gradually accumulated in the downstream region behave to preserve the thermal energy with time.

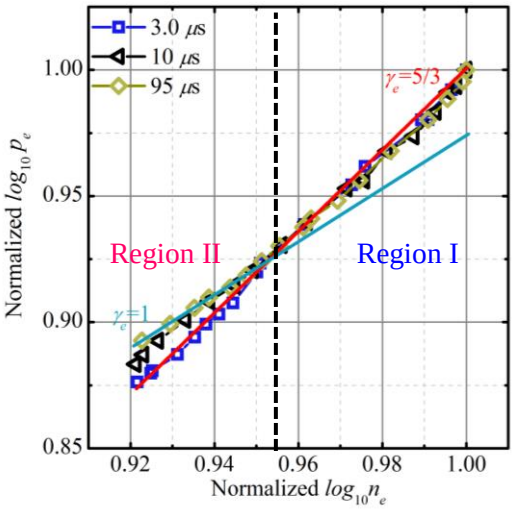

Figure 4.4. Log-log relationship between the effective electron pressure p_e and n_e. Polytropic curves with an exponent of 5/3 (solid red) and unity (solid cyan-green) represent the adiabatic and isothermal process, respectively.

Consequently, when total electrons are regarded as a single system in the MN, temporal changes in γ_e can be introduced; the expansion along entire axial distance follows the polytropic law with $\gamma_e = 1.58$ at $3.0\ \mu s$ and it reduces to $\gamma_e = 1.39$ at $95\ \mu s$. Thus, it is implied that as the thermal energy conserved electrons occupy most of the expansion region, the electron thermodynamics estimated for the entire expansion region can be seen as the isothermal process. It should be noted that the magnetically expanding electrons involved in the electric field generation behaves adiabatically.

The trapping of the cooled electrons via the effective potential structure is somewhat similar to the cut off effect during the afterglow of pulsed plasmas [59]. In general, the sequential diffusive cooling process of the electrons observed in the afterglow plasma is as follows: 1) the rapid loss of the energetic electrons results in the reduced plasma potential due to overall positive space charge, and 2) previously trapped electrons can overcome the reduced plasma potential and freely escape to the wall. In present study, the process we are interested in observing can be regarded as the reverse process to this; the effective potential structure generated by the adiabatic process of electrons gradually produces trapped electrons.

Table 3. Time scale during dynamic expansion and trapping of electrons.

	Fast Electron Cooling	Region I and Region II	Region II
Time	$3\ \mu s$	$0-10\ \mu s$	$10-17\ \mu s$
Process	✓ Fast expansion and cooling due to existence of ambient plasma;	✓ **Adiabatic process** ➢ Time scale of electric field formation in the expansion region ➢ Ion response time $\tau_i \sim 15\ \mu s$ after fast electron expansion [62,63] ✓ **Gradual formation of trapped region** ➢ Appearance of isothermally behaving trapped electrons ➢ Ionization and momentum transfer collisions with atom [61] ➢ $\tau_{en,ion} \sim 5\ \mu s$; $\tau_{en,elastic} \sim 0.3\ \mu s$	✓ **Region II: Disconnected from source region (electrons cannot reflect to source)** ➢ Fast electron bounce motion in the maximum magnetic moment well [61] ➢ Evolution of EEPF during electron-atom collision [61] ➢ Gradient of n_e and T_{eff} is disappeared ➢ Transition to a new equilibrium state in Region II separated from the source ($\tau_i \sim 10\ \mu s$)

- $\tau_{en,ion}$; ionization collision time, $\tau_{en,elastic}$; elastic collision time, $\tau_{escaping}$; escaping time, and τ_{Max}; Maxwellianization time [64].
- $\tau_{Max}\ (\sim 340\ \mu s) > \tau_{escaping}\ (\sim 200\ \mu s)$; average time required for an electron to suffer a 100% change in energy through electron-electron collisions is longer than particle escaping time.

Chapter 5. Conclusion

In this thesis, we clearly show that the isothermally behaving electrons which are trapped in a potential well formed by a combination of external magnetic field and ambipolar potential exists together with adiabatically expanding electrons ejected from the nozzle throat. Using their distinctive EEPF characteristics, we successfully explain the evolution of EEPFs from Maxwellian to non-Maxwellian distribution with superimposed low-energy electrons near the nozzle throat. Most importantly, the time-dependent kinetic property of the magnetically expanding plasma has been examined through the time-resolved measurement of the EEPFs. The developed effective potential well results in the trapping of the cooled electrons during the expansion process and shortens the magnetic expansion zone toward the nozzle throat (i.e., generating inaccessible region in the downstream). As a result, the change of the EEPFs represented as the accumulation of the trapped electrons during expansion causes a spatial change in γ_e that becomes closer to unity as it approaches to the downstream. Until now, the non-adiabatic behavior has been believed to the presence of a heat flux from the plasma source to the downstream region, so that the combination of the polytropic equation and the momentum equation could determine an asymptotic value of the potential of the entire expansion region. However, unlike the previous studies regarding the subject of the heat transfer as a plasma source region, this study emphasizes that the non-adiabatic behavior of an electron system is the main result of the trapped electron group generated in the local region disconnected to the source. Especially, this study is significant to present a new perspective that various values of polytropic index observed in the laboratory MN of each research group could be the result of the difference in bounce region of the isothermally behaving trapped electrons and gradual disconnection of the downstream from the source region determined by the strength and configuration of the magnetic field. Especially, the disconnection reduces the nozzle efficiency; the stagnation of the isothermal electrons in a limited region decreases the initially generated electric field in the downstream

region. From another point of view, our results indicate that it is possible to control the EEPF within the magnetically expanding plasma by changing the bounce region of trapped electrons according to the magnetic field conditions or pulse operation which prohibiting the electric field reduction effect in the downstream region. This study has great significance in that it is capable of explaining the formation of non-locally behaving Druyvesteyn-like distribution, which has been consistently observed in the research groups worldwide, as well as the locally behaving Maxwellian distribution found in other groups with the consideration of the non-locally behaving trapped electrons.

Bibliography

[1] R. G. Jahn, Physics of electric propulsion. (McGraw-Hill, New York, 1968).

[2] D. A. Kaufman, D. G. Goodwin, and J. C. Sercel, 29th Joint Propulsion Conference and Exhibit (1993).

[3] C. Charles and R. W. Boswell, Appl. Phys. Lett. **82**, 9 (2003).

[4] R. W. Boswell and E. Marsch, and C. Charles, Astrophys. J. **640**, L199 (2006).

[5] A. V. Arefiev and B. N. Breizman, Phys. Plasmas **15**, 042109 (2008).

[6] C. Charles, J. Phys. D **42**, 16 (2009).

[7] O. V. Batishchev, IEEE Trans. Plasma Sci. **37**, 8 (2009).

[8] B.W. Longmier et al., Plasma Sources Sci. Technol. **20**, 015007 (2011).

[9] J. P. Hughes et al., Astrophys. J. **327**, 615 (1988).

[10] M. Kartalev, M. Dryer, K. Grigorov, and E. Stoimenova, J. Geophys. Res. **111,** A10107 (2006).

[11] R. M. Skoug et al., J. Geophys. Res. **105**, A10 (2000).

[12] A. V. Arefiev and B. N. Breizman, Phys. Plasmas **16**, 055707 (2009).

[13] E. Ahedo and J. N. Cavalle, Phys. Plasmas **20**, 043512 (2013).

[14] M. Merino and E. Ahedo, IEEE Trans. Plasma Sci. **43**, 1 (2015).

[15] J. P. Sheehan et al., Plasma Sources Sci. Technol. **23**, 045014 (2014).

[16] R. W. Boswell, K. Takahashi, C. Charles and I. D. Kaganovich, Front. Phys. **3**, 14 (2015).

[17] S. A. Cohen et al., Rev. Sci. Instrum. **61,** 11 (1990).

[18] K. Takahashi et al., Phys. Rev. Lett. **107,** 235001 (2011).

[19] K. Takahashi, A. Chiba, A. Komuro, and A. Ando, Phys. Rev. Lett. **114,** 195001 (2015).

[20] K. Takahashi and A. Ando, Plasma Phys. Control. Fusion **59,** 054007 (2017).

[21] Cohen S A et al., Phys. Plasmas **10,** 2593 (2003).

[22] C. Charles and R. W. Boswell, Appl. Phys. Lett. **82**, 1356 (2003).

[23] C. Charles, Plasma Sources Sci. Technol. **16**, R1 (2007).

[24] K. Takahashi, Y. Itoh, and T. Fujiwara, J. Phys. D. Appl. Phys. **44**, 015204 (2011).

[25] K. Takahashi, A. Chiba, A. Komuro, and A. Ando, Plasma Sources Sci. Technol. **25**, 055011 (2016).

[26] A. Fruchtman, IEEE Trans. Plasma Sci. **39**, 1 (2011).

[27] E. Ahedo, M. Merino, Phys. Plasmas 18, 053503 (2011).

[28] D. M. Goebel and I. Katz, Fundamentals of Electric Propulsion: Ion and Hall Thrusters (Wiley, New York, 2008).

[29] J. M. Little, Ph.D. thesis, Princeton University (2015).

[30] G. Sanchez-Arriaga, J. Zhou, E. Ahedo, M. Martinez-Sanchez, and J. Ramos, Plasma Sources Sci. Technol. **27**, 035002 (2018).

[31] S. A. Andersen, V. O. Jensen, P. Nielsen, and N. D'Angelo, Phys. Fluids **12**, 557 (1969).

[32] M. A. Raadu, Plasma Phys. **21**, 331 (1979).

[33] M. Dryer, J. Geophys. Res. **76,** 4 (1971).

[34] M. Martinez-Sanchez, J. Navarro-Cavalle and E. Ahedo, Phys. Plasmas **22**, 053501 (2015).

[35] J. Navarro-Cavalle, S. Correyero, and E. Ahedo, Proceedings of 34th International Electric Propulsion Conference, Kobe, Japan, July 4 –10, 2015, IEPC-2015-117 (IEPC, Kobe, 2015).

[36] Y. Hu, J. Wang, IEEE Trans. Plasma Sci. **43**, 9 (2015).

[37] M. Merino and E. Ahedo, IEEE Trans. Plasma Sci. **43**, 1 (2015).

[38] M. Merino and E. Ahedo, Encyclopedia of plasma technology. (Taylor & Francis, 2017).

[39] I. Masaaki, et al., J. Plasma Fusion Res. **78**, 12 (2002).

[40] J. M. Little and E. Y. Choueiri, Phys. Rev. Lett. **117**, 225003 (2016).

[41] Y. Zhang, C. Charles and R. W. Boswell, Phys. Rev. Lett. **116**, 025001 (2016).

[42] I. I. Litvinov, J. Appl. Mech. Tech. Phys. **12**, 793 (1953).

[43] Y. Zhang, C. Charles and R. W. Boswell, Astrophys. J. **829**, 10 (2016).

[44] K. Takahashi, C. Charles, R. W. Boswell, A. Ando, Phys. Rev. Lett. **120**, 045001 (2018).

[45] K. S. Chung et al., Fusion Eng. Des. **109**, 454 (2016).

[46] E. Ahedo, Phys. Plasmas **18**, 103506 (2011).

[47] Ebersohn, F. H. Ph. D. thesis; Texas A&M University (2012).

[48] F. F. Chen, *Plasma Diagnostic Techniques*, (Academic, New York, 1965).

[49] R. C. Woods, and I. D. Sudit, Phys. Rev. E. **50**, 3 (1994).

[50] Lieberman M A and Lichtenberg A J 2005 Principle of Plasma Discharges and Materials Processing (New York: Wiley).

[51] V. A. Godyak, and V. I. Demidov. J. Phys D: Appl. Phys. **44**, 233001 (2011).

[52] K. Dannenmayer and P. Mazouffre, Plasma Sources Sci. Technol. **22**, 035004 (2013).

[53] R. W. Callis and D. T. Tuma, IEEE Trans. Plasma Sci. **2**, 283 (1974).

[54] X. Zhang et al., Phys. Plasmas **25**, 023503 (2018).

[55] P. Mora, Phys. Rev. Lett. **90**, 185002 (2003).

[56] C. Chan et al., Phys. Fluids **27**, 266 (1994).

[57] G. Hairapetian and R. L. Stenzel, Phys. Fluids **3**, 899 (1991).

[58] J. Y. Kim et al., New J. Phys. **20**, 063033 (2018).

[59] A. Maresca, K. Orlov, and U. Kortshagen, Phys. Rev. E **65**, 056405 (2002).

[60] J. Y. Kim et al., Plasma Sources Sci. Technol. **28**, 07LT01 (2019).

[61] I. Kaganovich, M. Misina, S. V. Berezhnoi, and R. Gijbels, Phys. Rev. E **61**, 2 (2000).

[62] N. Singh and R. W. Schunk, J. Geophys. Res. **87**, 9154 (1982).

[63] U. Samir, K. H. Wright, N. H. Strone, Rev. Geophys. Space Phys. **21**, 7 (1983).

[64] C. Thaury, P. Mora, J. C. Adam, and A. Heron, Phys. Plasmas **16**, 093104 (2009).

Abstract in Korean

자기적으로 팽창하는 플라즈마에서 전자의 동적 팽창 및 구속 연구

김 준 영
에너지시스템공학부
(핵융합 및 플라즈마 공학 전공)
서울대학교 대학원

천체물리학에서 우주 추진체 목적의 응용 분야에 이르기까지 광범위한 분야의 플라즈마 분석에 있어, 팽창하는 자기장 내 플라즈마의 거동 특성을 이해하는 것은 중요하다. 이 점에서 우주 플라즈마와 유사한 특성을 보이는 자기 노즐 장치는 다양한 실험 및 이론적 연구 결과를 제공하여 자기적으로 팽창하는 플라즈마의 깊은 이해를 돕는다.

전자 운동량으로부터 이온의 운동 에너지로의 변환은 자기 팽창 플라즈마의 대표적인 물리적 특성이며, 따라서 노즐 장치에서 열역학적 접근 방식을 기반으로 한 전자의 운동 특성에 대한 심도 높은 이해는 플라즈마의 근본 성질 파악에 직접적으로 기여한다. 본질적으로, 무충돌 조건에서 발산 자기장을 통한 전자 변수의 변화는 폴리트로픽 방정식을 통하여 표현 가능하며, 전자의 열역학적 상태는 외부와의 열 교환이 차단된 폴리트로픽 지수(γ_e)가 5/3 인 단열 과정으로 예상되었다. 하지만 태양풍 및 자기 노즐 장치에서 수행된 실험과 전산 모사에서, 팽창하는 자기장을 따라 측정된 플라즈마 변수들의 선형 회귀 분석은 단열($\gamma_e = 5/3$)보다 작고, 등온($\gamma_e = 1$)에 더욱 가까운 특성을 보였다. 관찰된 전자의 비단열적 특성에 대한 연구 그룹들의 이론적 접근 방식은 각 그룹의

결과들을 독자적으로 해석하는데 성공적이었지만, 그 해석들을 다른 그룹에 적용시킬 수 없었으며, 결국 이론적 합의에 도달하지 못하였다.

본 연구에서는 자기 노즐 장치에 공급되는 자기장과 전자의 거동으로 생성된 전기장의 결합에 의하여 형성된 자기 거울이 왕복 운동을 하는 속박된 전자를 생성할 수 있다는 관점에서 전자 열역학적 분석이 수행된다. 자기 노즐 장치의 팽창 영역에 존재 가능한 전자 그룹들을 선택적으로 수집할 수 있도록, 양면 평면 랭뮤어 탐침을 사용하여 전자 에너지 확률 분포 함수를 획득하며, 등온 특성을 가지는 속박된 전자와 $\gamma_e = 5/3$ 인 단열 팽창을 하는 전자가 공존함을 밝힌다. 자기 노즐 내의 단열 팽창하는 전자와 함께 등온적으로 행동하는 속박된 전자의 존재는 자기 노즐 시스템을 상이한 열역학적 성질을 갖는 두 개의 영역으로 분리시킨다; 하나는 노즐 목 근처에 위치한 단열 팽창 영역이고 다른 하나는 하류에 위치한 등온 영역이다. 자기장의 세기 변경에 따른 전자 열역학적 특성의 변화는 변경된 최대 전자 자기 모멘트의 공간적 형태로 설명될 수 있다. 궁극적으로 본 연구는 자기 노즐의 열역학적 특성이 단열 팽창을 수행하는 전자 그룹과 더불어 등온적으로 거동하는 전자에 의하여 영향을 받기 때문에 자기적으로 팽창하는 플라즈마의 특성이 γ_e 로 직접적으로 추론되어서는 안된다는 것을 주장한다.

또한, 우리는 최근의 연구 그룹들의 실험 방식이 정적 관측에 국한되어 왔으며, 이러한 실험적 한계가 전자의 열역학 특성의 차이에 관한 원인 분석을 제한했다는 사실에 중점을 둔다. 이 문제에 대응하여 전자 에너지 확률 분포 함수의 시간적 변화를 관찰함으로써 자기 노즐에서 자기적으로 팽창하는 플라즈마의 시간 의존적인 운동 특성을 밝히고 전자 열역학을 분석하기 위하여 일련의 팽창 과정을 파악한다. 팽창의 과정에서 생성된 전기장에 의하여 점진적으로 형성되는 자기 거울은 전자 운동의 제한 요인으로 작용한다는 것이 밝혀졌다. 이 효과는 속박 전자의 축적으로 대표되는 전자 에너지 분포 함수의 변화를

일으키며, 전자의 자기 팽창 영역을 노즐 입구 쪽으로 단축시킨다. 속박 전자의 축적은 시스템의 냉각 정도를 감소시키며, 초기 단열 확장에 의하여 생성된 하류 영역 전기장은 소스와의 단절 효과로 인하여 감소된다.

본 연구는 공간적으로 변경되는 전자의 열역학적 상태의 근본적인 원인을 제시해 줄 뿐만 아니라 자기적으로 팽창하는 플라즈마의 운동 특성이 구속 전자의 비정적 거동에 영향을 받는다는 것을 증명한다. 따라서 구속 전자의 시간에 따른 운동 특성 변화는 자기적으로 팽창하는 플라즈마의 특성 파악을 위한 필수적인 요소임을 강조하며, 나아가 공학적 응용 관점에서 점진적으로 생성되는 단절 영역에 의한 전기장 감소 현상을 효과적으로 제어해야 할 필요성을 제기한다.

Keywords; 자기 팽창 플라즈마, 자기 노즐, 전자 열역학, 비단열적 거동, 자기 미러, 전자 에너지 확률 분포,

학 번: 2015-30290